Generation of Random Geological Models Using Multi-Randomization for Machine Learning

Kai Gao* and Ting Chen

Earth and Environmental Sciences Division, Los Alamos National Laboratory, Los Alamos, NM 87544

*Corresponding author, kaigao@lanl.gov

The preprint was submitted to Computers & Geosciences for peer review. The structure and content of the preprint may change during the peer-review process.

The work is approved for public release under LANL approval LA-UR-25-27984.

Generation of Random Geological Models Using Multi-Randomization for Machine Learning

Kai Gao[a], Ting Chen[a]

[a]*Earth and Environmental Sciences Division, Los Alamos National Laboratory, Los Alamos, NM 87545, USA*

ARTICLE INFO

Keywords:
random geological model
machine learning
seismic image
geological fault
automated seismic interpretation

ABSTRACT

Generating high-fidelity geological models is essential for advancing machine learning (ML) methods in automated seismic interpretation. For instance, seismic images paired with corresponding fault labels are foundational for ML-based fault detection from seismic migration sections. While several open-access datasets of random geological models exist, open-source tools specifically designed to produce large volumes of such models for ML applications remain scarce. To address this gap, we present RGM (Random Geological Model), an open-source software package for efficiently generating 2D and 3D synthetic geological models tailored for ML workflows. RGM supports the creation of diverse model components, including medium property distributions (P-/S-wave velocities and density), seismic reflectivity images (i.e., synthetic migration sections), relative geological time, and discrete fault attributes such as probability, dip, strike, rake, and displacement. It also accommodates the creation of complex geological features such as salt bodies and unconformities. The model generation algorithm employs a multi-randomization strategy, yielding an effectively infinite-dimensional model space that encompasses a wide range of geological scenarios and associated seismic features. Furthermore, RGM incorporates a method to generate synthetic elastic migration images using analytical elastic reflection coefficients combined with frequency-dependent scaling. This functionality enables the creation of training datasets for ML models that leverage elastic seismic images. RGM is implemented in modern object-oriented Fortran, allowing users to flexibly control statistical parameters governing model variability. We demonstrate the capability, performance, and geological realism of the package through comprehensive 2D and 3D examples.

CRediT authorship contribution statement

Kai Gao: Conceptualization; Methodology; Software; Formal Analysis; Visualization; Writing – original draft; Funding Acquisition; Resources. **Ting Chen:** Writing – review & editing; Funding Acquisition; Resources; Project Administration.

1. Introduction

Machine learning (ML) methods are automating seismic interpretation in recent years. Numerous supervised or semi-supervised ML models have been developed for automatically identifying faults (Di et al., 2018; Wu et al., 2019a; Wang et al., 2024; Gao, 2024), seismic horizons and relative geological time (RGT) (Tschannen et al., 2020; Geng et al., 2020; Bi et al., 2021), salt bodies (Guo et al., 2021; Zhang et al., 2022), channels (Pham et al., 2019; Gao et al., 2021), seismic stratigraphy (Di et al., 2020), and so on, some of which are multitask (Wu et al., 2019b, 2023; Gao, 2024). See Lin et al. (2024) for a comprehensive review of these models and prospects of this field.

One of the key factors to obtaining generalizable ML models for these tasks is high-quality seismic data (seismic images, fault labels, and other relevant seismic attribute images). In fields such as computer vision and natural language processing (NLP), the availability of large-scale open-access datasets – such as images, videos, audio, and text – has

---

ORCID(s): `0000-0002-3280-8181` (K. Gao) been a major driver of ML progress (e.g., Deng et al., 2009), with many datasets containing millions of examples. In contrast, ML applications in automated seismic interpretation have struggled with a shortage of high-fidelity labeled data. Wu et al. (2019c) and Wu et al. (2019d) demonstrated that it is feasible to use solely synthetic seismic images for training fault detection ML model. The idea was later validated in broader applications, including seismic image denoising (Li et al., 2022), RGT inference (Geng et al., 2020; Bi et al., 2021), fault detection (Gao et al., 2022a,b; Wang et al., 2024), fault geometric attribute inference (Wu et al., 2019d; Gao, 2024; Gao and Chen, 2025), and so on.

Generation of synthetic seismic images and subsurface attributes lies in the domain of geological modeling (Wu and Xu, 2003; Caumon et al., 2009; Georgsen et al., 2012; de la Varga and Wellmann, 2016; de la Varga et al., 2019). Explicit geological modeling methods (e.g., Wu and Xu, 2003) and implicit methods (e.g., Calcagno et al., 2008; de la Varga et al., 2019) have found wide applications but are not designed specifically for generating a large amount of random geological models (especially seismic images and fault/fault attribute labels) for automatic seismic interpretation applications. Wu et al. (2019a) developed a procedure for generating synthetic seismic images and fault labels. Wu et al. (2020) presented an improved procedure to generate synthetic seismic images and faults. The method improves the fidelity of fault surfaces by introducing spatially decaying fault displacement on a fault surface and generating curved or listric fault surfaces through random surface perturbation. However, the sedimentary layer perturbation in this work is restricted to folding structures by summing from random Gaussian functions. In the same work, as well as later works by Geng et al. (2020) and Bi et al. (2021), the authors developed methods for generating synthetic RGT attribute along with seismic images and fault labels, and trained ML models to infer RGT from seismic images. Wang et al. (2023) developed a 3D geological modeling workflow for generating random geological models. In addition to applying random perturbation to fault surfaces as in Wu et al. (2020), they develop procedures to simulate fault displacement and fault drag (Grasemann et al., 2005) to better replicate realistic geological faults. The output from the method, however, only contains a seismic reflectivity image and a fault probability image. Lin et al. (2025) developed a parametric modeling method to generate random geological models for ML applications. These aforementioned works provide open-access datasets but the geological model generation algorithms themselves are not open-source, imposing nontrivial limitations for data reproducibility and adaption to specific geological regions or models of different sizes (e.g., synthetic images and fault labels with dimensions other than $128 \times 128 \times 128$).

Our work aims specifically to develop an open-source, modern Fortran-based, high-performance package for generating synthetic random geological models, with a focus on computational efficiency, geological realism, and data reproducibility. Our package, named Random Geological Model (RGM), can generate faulted random medium parameter models (P-wave velocity, S-wave velocity, and density models), facies (piecewise constant chronological model), RGT (piecewise smooth chronological model), faults (indexed from 1 to maximum number of faults in a model) and fault attributes (including dip, strike, rake, and displacement), salt bodies, and unconformity. The procedure used in our open-source package is inspired by and similar to the workflows developed by Wu et al. (2019a), Wu et al. (2020), and Lin et al. (2025), but also with some notable differences and important feature improvements.

First, we use two bounding surfaces at the top and the bottom for generating layer interfaces and positions. These surfaces can simulate both smooth and abrupt variations of sedimentary layers to improve geological realism of a generated model. Second, we adopt a simplified and efficient approach to insert faults into a random model, and design two strategies for creating faults (including faults with random orientations and faults with grouped orientations) to mimic topology of realistic fault networks. Specially, recognizing the importance of listric faults (Georgsen et al., 2012; Shafiq et al., 2018; Wu et al., 2020), we develop a straightforward method for inserting curved faults with depth-decaying dip angles in a random geological model to improve geological realism. The method is different from the volumetric vector field approached developed by Georgsen et al. (2012), but the resulting model is visually plausible from a structural geology point of view. Third, we introduce a new method for insert one or more random unconformity surfaces to a random model along with a systematic method to adjust RGT values after insertion of unconformity surfaces. We also introduce a novel method to build one or more random salt bodies to a random model using randomized circular curves combined with monotonic spline interpolation. These functionalities improve the realism and applicability of resulting random models compared with existing works where no unconformity or salt body exists, such as the method by Wu et al. (2020). Fourth, we provide the functionality to insert one or multiple unconformity surfaces into the model that can mimic disconformity, nonconformity, and angular unconformity in realistic geology.

In RGM, we generate geological models by assigning randomized values to the parameters that define individual geological features, where each feature (e.g., layer, faults, salt bodies, or unconformities) uses an independent randomization realization to ensure variability and uniqueness. This multi-randomization framework ensures that the resulting models maintain geological plausibility while avoiding repetitive or overly deterministic patterns, making RGM particularly suitable for generating large amounts of data for training of ML models of automated seismic interpretation. With the open-source implementation of our algorithm, users can generate a wide range of randomized geological models by customizing dozens of parameters to suit the specific requirements of their machine learning training tasks.

2. Methodology

2.1. Medium property models

We first generate layers for the random geological model. We use the following steps to build an unfaulted model.

Step 1: Generate top and bottom bounding surfaces that constrain overall shapes of the layers. We set two random surfaces to represent the top-most and bottom-most reflectors, and each of them can be one of the following surfaces:

1. Smoothed random surface defined by

$$I(x, y) = \mathcal{G}_{\sigma_x,\sigma_y}(s(x, y)), \tag{1}$$

where $s(x, y)$ represents a 2D array filled with random values drawn from a uniform distribution, and the tunable parameters σ_x and σ_y represent the smoothing radii of the Gaussian filter $\mathcal{G}$ along the x- and y-axes, respectively. Figures 1a and b display an example of 1D smooth random interface (for generating 2D random geological model) and an example of 2D smooth random surface (for generating 3D random geological model).

2. Random Gaussian surface defined by

$$I(x, y) = \sum_{i=1}^{m} h_i \exp\left[-\frac{1}{2}\left(\left(\frac{x - \mu_{x,i}}{\sigma_{x,i}}\right)^2 + \left(\frac{y - \mu_{y,i}}{\sigma_{y,i}}\right)^2\right)\right], \tag{2}$$

where the parameters μ_x and μ_y control the locations of the Gaussian functions in the horizontal positions, σ_x and σ_y control the width of the Gaussian functions, and h_i controls the height of each Gaussian functions. With RGM, the user can set random values for these three parameters (μ, σ, and h) to generate a smooth, Gaussian surface or interface.

3. Random Cauchy surface defined by

$$I_3(x, y) = \sum_{i=1}^{m} h_i \left[1 + \left(\frac{x - \mu_{x,i}}{\sigma_{x,i}}\right)^2 + \left(\frac{y - \mu_{y,i}}{\sigma_{y,i}}\right)^2\right]^{-3/2}. \tag{3}$$

Under the same value of σ_x or σ_y, the Cauchy function appear sharper than the Gaussian function. Therefore, a random Cauchy surface can mimic more localized and more horizontally "compressed" fold structures than a Gaussian surface. Figures 1e and f display an example of 1D smooth Gaussian interface and an example of 2D smooth Gaussian surface. In RGM, both Gaussian and Cauchy random surfaces can rotate based on:

$$\begin{bmatrix} \hat{x} \\ \hat{y} \end{bmatrix} = \begin{bmatrix} \cos(\theta_i) & -\sin(\theta_i) \\ \sin(\theta_i) & \cos(\theta_i) \end{bmatrix} \begin{bmatrix} x - \mu_{x,i} \\ y - \mu_{y,i} \end{bmatrix}, \tag{4}$$

where θ_i is a random rotation angle on the $x - y$ plane for the i-th 2D Gaussian or Cauchy function. Substituting $x - \mu_x$ and $y - \mu_y$ with $\hat{x}$ and $\hat{y}$, respectively, we can then obtain the random surface to mimic rotated fold structures.

4. Multi-octave Perlin surface (Perlin, 1985; Etherington, 2022): To generate a 2D Perlin surface consisting of $N_x \times N_y$ grid points, we first divide the mesh into $M_x \times M_y$ coarse grids (M_x and M_y are usually called the

resolutions of a Perlin noise). We then randomly assign unit gradient vectors generated through $\mathbf{g} = (g_x, g_y) = [\cos(\phi), \sin(\phi)]$, where $\phi \in \mathcal{U}(0, 2\pi)$ is a set of random values drawn from the uniform distribution limited by a lower bound of 0 and an upper bound of 2π. For each fine-mesh grid point $\mathbf{p} = (x, y)$, we first locate their lower and upper integer bounding grid points $(x_0, y_0) = \lfloor x, y \rfloor$ and $(x_1, y_1) = \lceil x, y \rceil$, and then the corner values corresponding to $\mathbf{x}$ is computed based on the dot product between the random gradient vectors and the distance vectors:

$$v_{00} = g_{x,0}(x - x_0) + g_{y,0}(y - y_0), \tag{5}$$

$$v_{01} = g_{x,0}(x - x_0) + g_{y,1}(y - y_1), \tag{6}$$

$$v_{10} = g_{x,1}(x - x_1) + g_{y,0}(y - y_0), \tag{7}$$

$$v_{11} = g_{x,1}(x - x_1) + g_{y,1}(y - y_1). \tag{8}$$

Defining a fade function function as

$$f(t) = 6t^5 - 15t^4 + 10t^3, \tag{9}$$

and a linear interpolation as

$$\mathcal{L}(a, b, t) = a + t(b - a), \tag{10}$$

then we generate the Perlin noise at (x, y) as

$$P(x, y) = \mathcal{L}(\mathcal{L}(v_{00}, v_{10}, \delta x), \mathcal{L}(v_{01}, v_{11}, \delta x), \delta y), \tag{11}$$

where $\delta x = f(x - x_0)$ and $\delta y = f(y - y_0)$. Repeating the procedure for all the fine-mesh grid points, we then obtain the Perlin noise at this octave. Furthermore, a multi-octave Perlin noise can be generated via

$$s(\mathbf{x}) = \sum_{i=0}^{N_v - 1} w^i P(\eta^i \mathbf{x}), \tag{12}$$

where $w \in (0, 1]$ is call the persistence for decreasing the amplitude of noise over octaves, η is the lacunarity for increasing the spatial frequency of noise over octaves, and N_v is the number of octaves; in our implementation, for simplicity we use $\eta = 2$ and $w = 0.5$. Figures 1g and h display an example of 1D smooth Perlin interface and an example of 2D smooth Perlin surface.

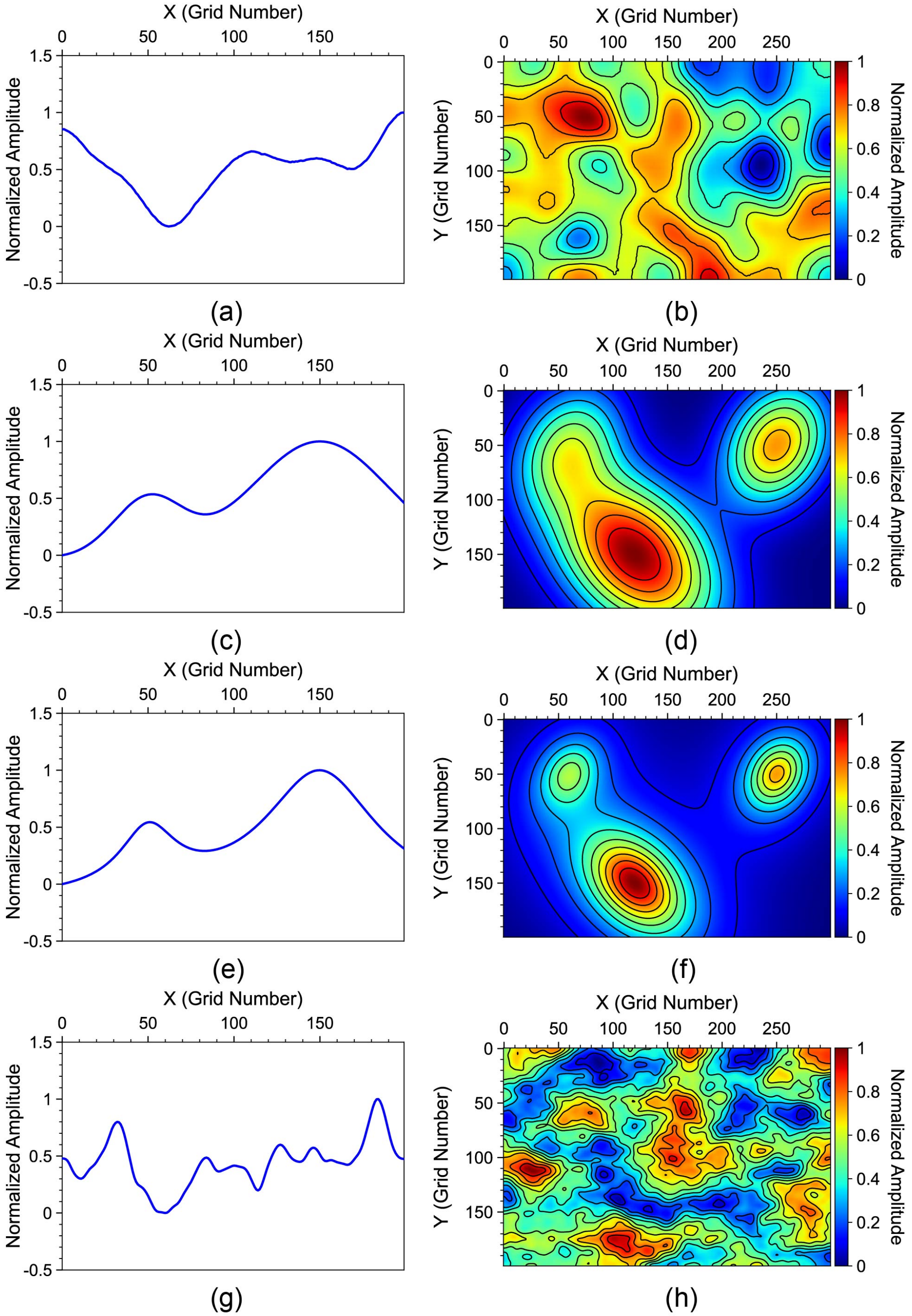

Figure 1: Examples of random interfaces and surfaces serving as bounding surfaces in RGM, including (a-b) smoothed random surfaces, (c-d) random Gaussian surfaces, (e-f) random Cauchy surfaces, and (g-h) random Perlin surfaces.

We then add a linear slope to the generated interface:

$$I'(x, y) = I(x, y) + \frac{x}{x_{\max}} \Delta L_x + \frac{y}{y_{\max}} \Delta L_y, \tag{13}$$

where the tunable parameters ΔL_x and ΔL_y are the maximum slopes along the x- and y-axis, respectively, and $x_{\max}$ and $y_{\max}$ represent the maximum dimensions of the model in the x and y directions, respectively.

Step 2: Compute in-between reflector positions. We use linear interpolation to compute the coordinates $z_i(x, y)$ of the i-th reflector in the vertical direction:

$$\frac{z_i(x, y) - z_1(x, y)}{z_n(x, y) - z_1(x, y)} = \frac{i-1}{n-1}, \tag{14}$$

where n represents the number of interfaces in total, and (x, y) represents the horizontal coordinates of a point on the i-th reflector.

We introduce a vertical thickness variation to the generated layer positions. We first compute the first-order derivative of z_i along the vertical direction at every horizontal position, and the resulting derivative is the thickness of the layers. We then multiply the layer thickness with a 1D random array with values drawn from a uniform distribution $\mathcal{U}(1-\delta_v, 1+\delta_v)$, where $0 \leq \delta_v \leq 1$ is a hyper-parameter that can be defined by the user. We then integrate the randomly weighted array to obtain the adjusted layer thicknesses, which vary randomly in the vertical direction. Assuming the sequence of vertical positions of the uniform-thickness layers at the horizontal position (x, y) is $l(x, y) = \{z_1(x, y), z_2(x, y), \cdots, z_n(x, y)\}$, then the vertical positions of the layers after adjustment can be written as:

$$z'_i(x, y) = \int_1^i \left[w_\zeta \max\left(0, \frac{\tilde{\partial} l(x, y)}{\tilde{\partial} \zeta}\right)\right]_{\hat{\zeta}} d\zeta, \tag{15}$$

where ζ represents the vertical axis, w_ζ represents the depth-varying weights, and $\hat{\zeta}$ represents the discrete values of layer thickness after weighting. Note that here because $l(x, y)$ is a discrete function, we use the symbol $\tilde{\partial}$ to represent a finite-difference approximation to the continous derivative. Assuming the layer position in the vertical direction is $l'(x, y) = \{z'_1(x, y), z'_2(x, y), \cdots, z'_n(x, y)\}$, then we linearly transform the adjusted vertical positions to the range of $[z_1, z_n]$ with

$$l''(x, y) = \frac{l' - l'_{\min}}{l'_{\max} - l'_{\min}} \left[z_n(x, y) - z_1(x, y)\right] + z_1(x, y), \tag{16}$$

A sedimentary layer may also have varying thickness across the horizontal directions. By assuming the vertical positions of the layers are $h(x, y) = \{z'_1(x, y), z'_2(x, y), \cdots, z'_n(x, y)\}$, we introduce horizontal layer thickness variations via

$$z_i''(x,y) = \int_1^i \left[\max\left(0, \frac{\tilde{\partial}(h(x,y) + \mathcal{S}_\eta \circ \mathcal{G}_\sigma(r(x,y)))}{\tilde{\partial}\zeta}\right)\right]_{\hat{\zeta}} d\zeta, \tag{17}$$

where $\mathcal{S}_\eta$ represents a linear transform that transforms the input to $[-\eta, \eta]$ with η being the maximum perturbation of layer thickness in the horizontal directions, and varies from layer to layer because the thickness of each layer can be different after the vertical thickness layer adjustment discussed above. In addition, σ is the standard deviation of the Gaussian filter $\mathcal{G}$ for smoothing the random values $r(x,y)$. Again, here we use $\tilde{\partial}$ to represent a finite-difference approximation to the continuous vertical derivative.

After the layer thickness adjustment, we obtain the vertical positions of the layers as

$$l''(x,y) = \{z_1''(x,y), z_2''(x,y), \cdots, z_n''(x,y)\}. \tag{18}$$

We then linearly transform the positions to the range of (z_1, z_n) with:

$$z_i^{\text{final}}(x,y) = \frac{l'' - l''_{\text{min}}}{l''_{\text{max}} - l''_{\text{min}}} \left[z_n(x,y) - z_1(x,y)\right] + z_1(x,y). \tag{19}$$

Step 3: Fill layers with medium property values. The final step of creating an unfaulted geological model is to fill the grid points between the interfaces $\{z_i^{\text{final}}\}$ with values of the medium property (in our case, the P-wave velocity V_p). In our RGM, we use linear interpolation of $n-1$ distinct velocity values along the z direction to build this model. In specific, as displayed in Figure 2, because along the z-axis the interface points may not fall exactly on integer grid points, simply using the values from nearest grid points may create staircases in the generated model. Therefore, within each layer (i.e., between two reflectors z_i and z_{i+1}), we create n_l regularly sampled grid points as

$$\{z_i + \Delta z_i, z_i + 2\Delta z_i, \cdots, z_{i+1} - \Delta z_i\}, \tag{20}$$

where $\Delta z_i = (z_{i+1} - z_i)/(n_l + 2)$, and the corresponding medium property values for these n_l grid points are all $v_{i,i+1}$. Along the depth direction, we then resample the non-uniformly sampled sequence

$$\{\mathbf{Z}, \mathbf{V}\} = \{(z_1 + \Delta z_1, v_{1,2}), \cdots, (z_i + \Delta z_i, v_{i,i+1}), \cdots, (z_n - \Delta z_n, v_{n-1,n})\} \tag{21}$$

to uniformly sampled grids $0, 1, 2, .., N_z - 1$ using linear interpolation. We repeat the process for all the horizontal positions, and obtain the medium property values on the regular grid points that define the random geological model.

Figure 2 is a schematic plot of the above linear interpolation procedure to obtain medium property values on integer grid points that cover the final regular-grid geological model.

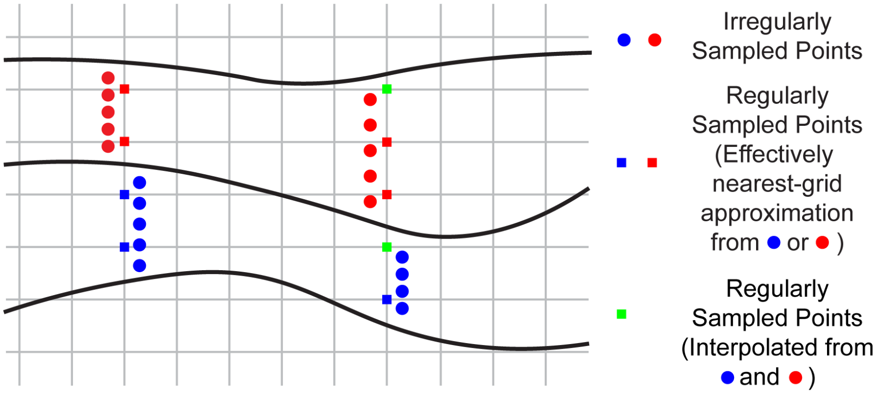

Figure 2: Interpolation of irregularly sampled layer velocity values (indicated by blue and red disks) onto a regularly sampled computational mesh (represented by blue, red, and green squares). For visual clarity, the disks are laterally offset from their corresponding mesh locations; in reality, they are horizontally aligned with underlying grid lines.

Because we may need to insert one or multiple faults with non-zero vertical displacements into the unfaulted model, it is important to pad additional grid points to the boundaries of the model. The added grid points must ensure that after the shiftings caused by faults, the most exterior grid points of the unfaulted model are not in the interior of the final faulted model, as indicated by the black and white rectangles in Figure 3. The number of padded layers should be as small as possible to reduce computational cost. We estimate the number of additional grid points required to pad a model along the z-axis (i.e., at the top and bottom surfaces of the model) as

$$m_1 = \max\left(\sum_{i=1}^{N_f} \max(f_{d,i}\sin(\theta_i), 0), -\sum_{i=1}^{N_f} \min(f_{d,i}\sin(\theta_i), 0)\right), \tag{22}$$

$$m_2 = \max(|\Delta L_x|, |\Delta L_y|), \tag{23}$$

$$m_3 = \max(|\Delta H_x|, |\Delta H_y|), \tag{24}$$

$$E_z = \lceil \max(m_1, m_2) + m_3 \rceil, \tag{25}$$

where $\lceil x \rceil$ represents the nearest integer larger than x, and ΔH_x and ΔH_y represent the maximum heights of top and bottom bounding surfaces, respectively. The above equations account for the maximum possible vertical shifts caused by N_f faults (the method for inserting faults into the model will be discussed in the next section), nonzero slopes, and heights of the reflectors.

Similarly, the number of grid points needed to pad the horizontal boundaries can be estimated as

$$m_1 = \sum_{i=1}^{N_f} \max(f_{d,i}(\cos(\varphi_i)\sin(\phi_i) - \sin(\varphi_i)\cos(\theta_i)\cos(\phi_i)), 0), \tag{26}$$

$$m_2 = -\sum_{i=1}^{N_f} \min(f_{d,i}(\cos(\varphi_i)\sin(\phi_i) - \sin(\varphi_i)\cos(\theta_i)\cos(\phi_i)), 0), \tag{27}$$

$$E_x = \lceil \max(m_1, m_2) \rceil, \tag{28}$$

$$m_3 = \sum_{i=1}^{N_f} \max(f_{d,i}(\cos(\varphi_i)\cos(\phi_i) - \sin(\varphi_i)\cos(\theta_i)\sin(\phi_i)), 0), \tag{29}$$

$$m_4 = -\sum_{i=1}^{N_f} \min(f_{d,i}(\cos(\varphi_i)\cos(\phi_i) - \sin(\varphi_i)\cos(\theta_i)\sin(\phi_i)), 0), \tag{30}$$

$$E_y = \lceil \max(m_3, m_4) \rceil. \tag{31}$$

The workflow for building an unfaulted model from two bounding surfaces is summarized in Figure 3.

In elastic wave modeling, imaging, and inversion applications, it is essential to build elastic wave velocity models including V_p and V_s in contrast to only V_p model in acoustic media. In some circumstances, one also needs to build a density model to accurately replicate reflection amplitudes. Our RGM provides functionality to generate V_s model based on a predefined range of V_p/V_s ratio $r_{\min} <= V_p/V_s <= r_{\max}$:

$$r = \frac{V_p - V_{p,\min}}{V_{p,\max} - V_{p,\min}}(r_{\max} - r_{\min}) + r_{\min}, \tag{32}$$

$$V_s = V_p/r. \tag{33}$$

It is worth noting that the computation of V_s model is performed after all faulting-related displacements are finished (the procedure is described in the Fault subsection).

In RGM, we generate a density model from V_p following Gardner's rule (Gardner et al., 1974).

2.2. Relative geological time

RGM can also generate piecewise smooth RGT attribute that is useful for inferring the sedimentary and deformation history of a region. Our RGM generates the unfaulted RGT volume in a similar way with the medium property model. In specific, we assume that RGT between two reflectors should be linearly decreasing from the lower reflector to the upper reflector, representing the older to newer sedimentation history, as indicated in Figure 4. In RGM, at every horizontal position (x, y), we linearly interpolate the layer depth positions $\xi_i = z_i^{\text{final}}(x, y)$ to the value range of $[0, N_z - 1]$ based

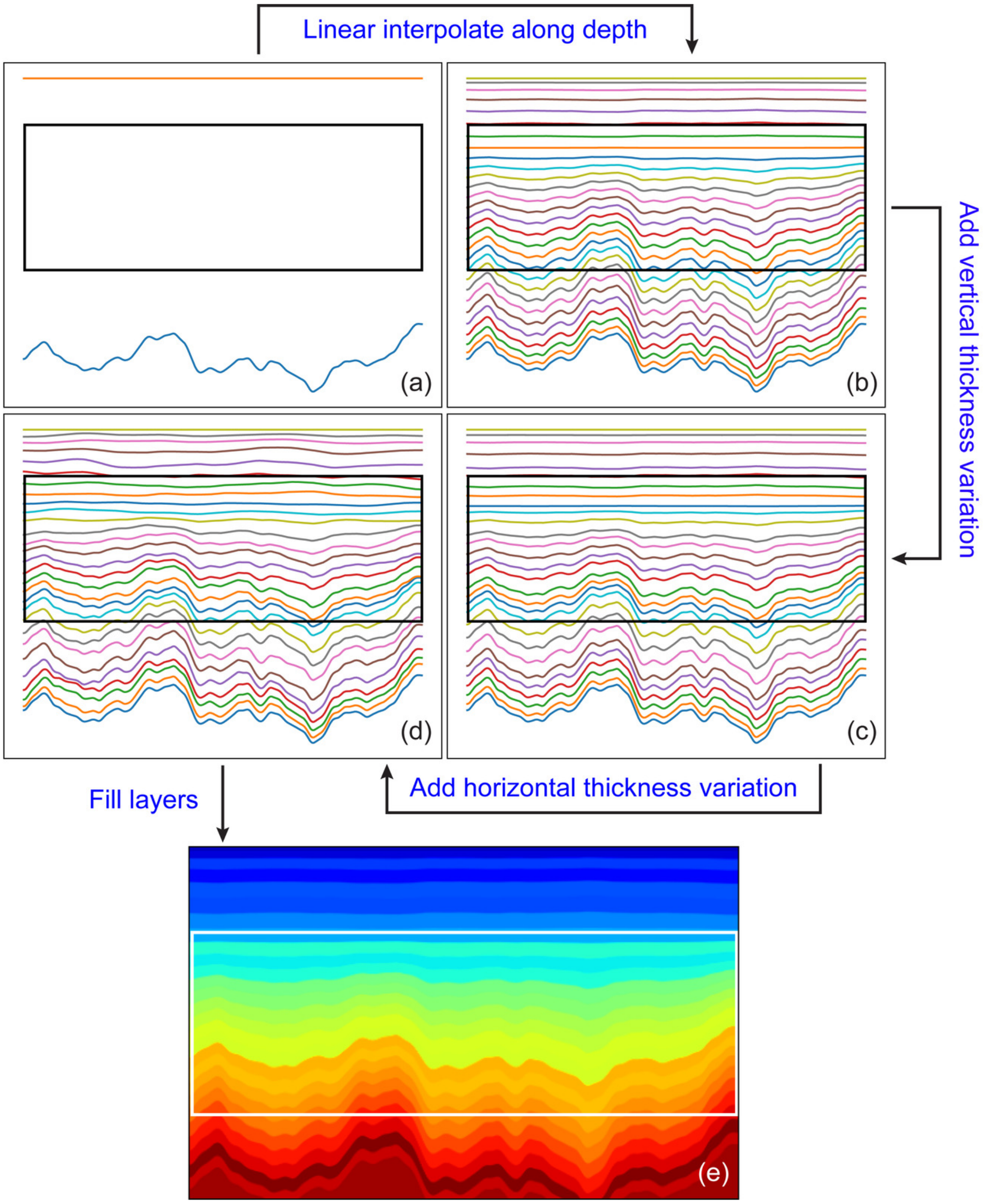

Figure 3: The workflow for generating the layer interfaces and filling layers with medium property parameters in RGM based on two bounding surfaces. The black rectangle in panels (a-d) (or the white rectangle in panel (e)) represent the region of the final geological model. The step of adding vertical thickness variation is based on equation (15), while the step of adding horizontal thickness variation is based on equation (17).

on stretched coordinates:

$$\mathbf{h} = \left\{N_z - 1 - \xi_1, N_z - 1 - \xi_2, N_z - 1 - \xi_3, \cdots, N_z - 1 - \xi_n\right\}, \tag{34}$$

$$\mathbf{z} = \left\{1, 1 - \frac{1}{n-1}, 1 - \frac{2}{n-1}, \cdots, 0\right\}, \tag{35}$$

$$\mathbf{h}' = \left\{0, 1, 2, \cdots, N_z - 1\right\}, \tag{36}$$

$$T(x, y) = \mathcal{L}(\mathbf{h}, \mathbf{z}, \mathbf{h}'). \tag{37}$$

where $\mathcal{L}$ represents linear interpolation that is built from the pairs $(\mathbf{h}, \mathbf{z})$ and interpolates at integer grid point locations $\mathbf{h}'$. Note that in most cases, $\mathbf{h}$ is a non-uniformly sampled sequence, because ξ (the depths of the reflectors) are adjusted by vertical and horizontal layer thickness variations. Therefore, the pairs $(\mathbf{h}, \mathbf{z})$ are equivalently coordinates stretching and compressing. The uniformly sampled sequence $\mathbf{h}'$ represents the coordinates of regularly sampled grid points that define the final random geological model.

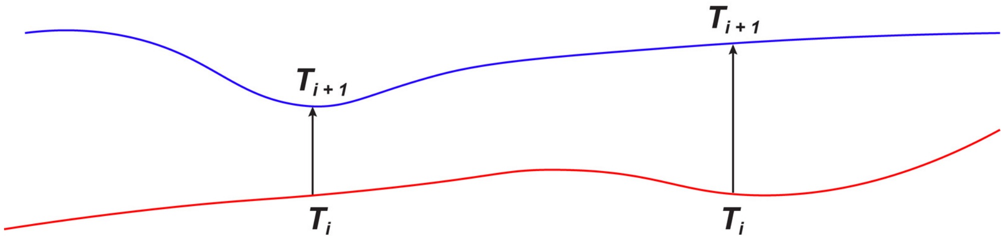

Figure 4: Schematic representation of RGT between two reflectors. The RGT values linearly decrease from T_i and T_{i+1} regardless of the layer thickness.

2.3. Faults

Faults are the key for our RGM to generate realistic geological models for training fault detection and characterization ML models. In RGM, instead of adopting the volumetric vector field approach (Cardozo et al., 2008; Georgsen et al., 2012; Laurent et al., 2013; Wu et al., 2020) for creating faults and shifting grid points, we develop a simpler approach.

We assume that for a fault surface (or a fault line in the 2D case), the displacement, strike, and rake are constant, while the dip can be constant (i.e., a planar fault surface) or can decrease smoothly from shallow to deep regions of the model (i.e., a listric fault surface). We display a comparison between straight and curved faults using a 2D example in Figure 5. In the implementation of RGM, we view the planar fault as a special type of curved fault with constant dip angle (i.e., $\theta(z_0) = \theta(z_{\max}) = \bar{\theta}$.

For a fault with a strike angle $\phi \in [0, \pi]$, a rake angle $\varphi \in [0, \pi]$, a displacement of δ, and a potentially depth-varying fault dip angle $\theta(z) \in (0, \pi)$, the horizontal deviation $(\delta x, \delta y)$ of the fault with respect to the topmost fault line at depth z is

$$\delta x = -\frac{1}{\tan(\theta(z))} \sin(\phi) z, \tag{38}$$

$$\delta y = \frac{1}{\tan(\theta(z))} \cos(\phi) z. \tag{39}$$

Assume the horizontal center of the fault is (f_x, f_y), and the fault has a strike angle of ϕ, then at the depth z, the line

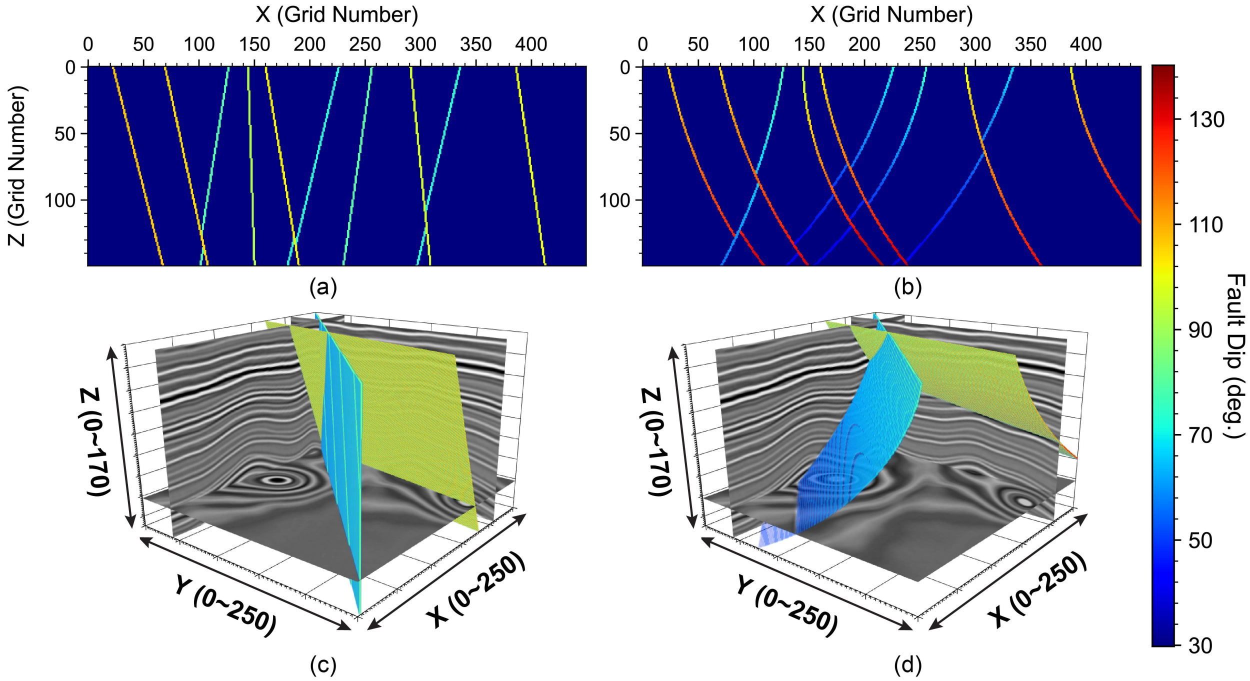

Figure 5: A comparison between (a, c) straight (planar) faults with depth-constant dip angles and (b, d) listric faults with depth-decaying dip angles (measured relative to the vertical) as generated by RGM.

representing the fault is

$$a = \tan(\phi), \tag{40}$$

$$b = (f_y + \delta y) - a(f_x + \delta x), \tag{41}$$

$$y = ax + b. \tag{42}$$

Therefore, the distance between any point $(\hat{x}, \hat{y})$ at depth z to the fault line $y = ax + b$ is

$$d = \frac{|\hat{y} - (a\hat{x} + b)|}{\sqrt{1 + a^2}}. \tag{43}$$

Consider that at the depth of z, the dip angle of a fault is $\theta(z)$, then in order for a grid point at the same depth being a fault point, the horizontal distance of this point to the fault line must satisfy $d_{x,y} \leq \frac{1}{2} f_w / \sin(\theta(z))$, where f_w is the thickness of the fault along its normal direction.

Equation (42) defines a series of fault lines on the $x - y$ plane along the depth axis. By checking the sign of the distance of a grid point to the fault line as indicated in Figure 6b, we obtain a block on one side of the fault, and this fault will be designated as the shifting block where grid points are to be moved, as indicated by the blue block in Figure 6c.

For every point in the model with a coordinate of (x, y, z) that falls into the shifting block, the spatial shift is

$$\Delta x = f_d[\cos(\varphi)\cos(\phi) - \sin(\varphi)\cos(\bar{\theta})\sin(\phi)], \tag{44}$$

$$\Delta y = f_d[\cos(\varphi)\sin(\phi) - \sin(\varphi)\cos(\bar{\theta})\cos(\phi)], \tag{45}$$

$$\Delta z = -f_d \sin(\varphi)\sin(\bar{\theta}), \tag{46}$$

where f_d is the fault displacement. Note that here $\bar{\theta}$ is a constant rather than a depth-varying quantity; in our implementation, we simply use the dip at $z = 0$ as the value of $\bar{\theta}$. Note that once the the block to be shifted is identified and the displacements along all three axes are determined, we shift the same set of grid point in all relevant models simultaneously, including the medium property model (V_p), the fault index model, the fault geometric attributes (dip, strike, rake, displacement) models, as well as the RGT model. By repeating the above procedure for N_f faults, each of which may have different values of dip, strike, rake, and displacement, we obtain a faulted geological model.

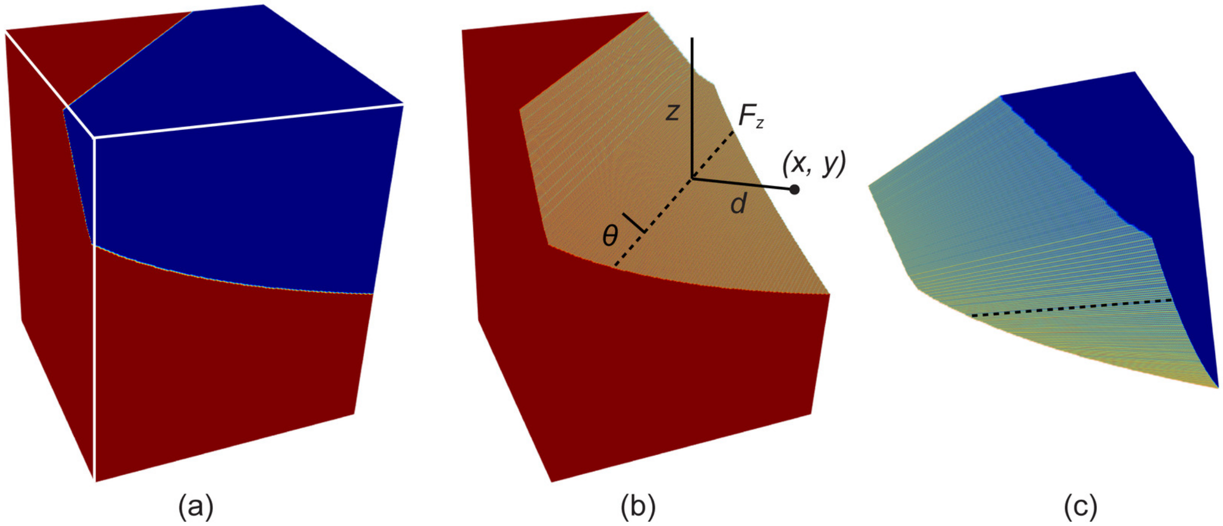

Figure 6: A schematic plot of creating a fault in RGM. F_z – the fault line at the depth of z; θ – the dip angle of fault at the depth of z; (x, y) – a grid point at the depth of z; d – shortest distance between (x, y) and F_z.

We design two ways to mimic realistic fault network topology: one is to generate relatively randomly distributed faults where the strikes, rakes, dips, and displacements for the individual faults can span a relatively wide value range as displayed in Figure 7a, and the other one is to generate relatively regularized faults grouped into two groups, where faults in each group have a similar strike, rake, dip, and displacement and are quasi-parallel with one another as displayed in Figure 7b.

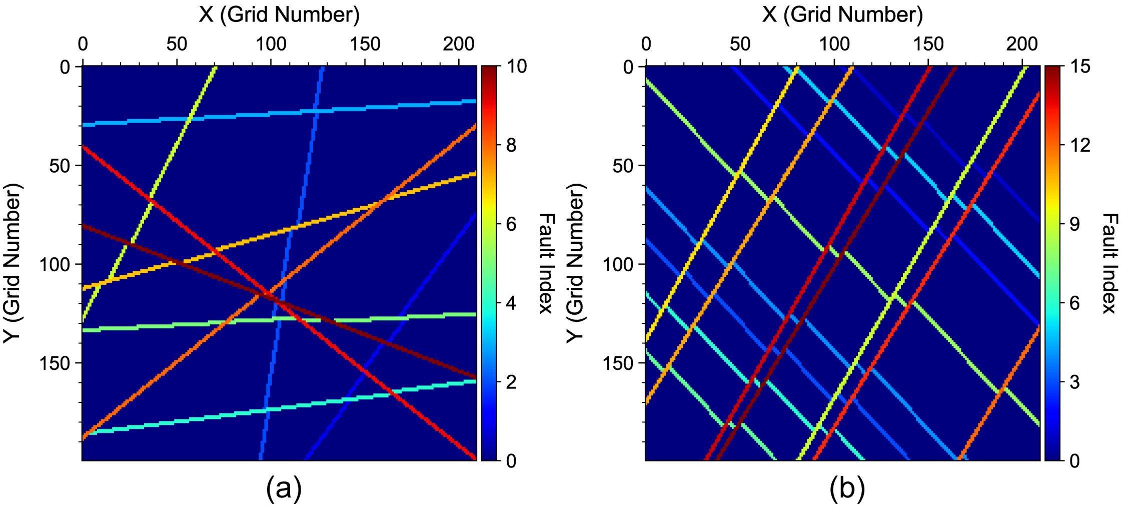

Figure 7: Map views of (a) faults with random strikes and (b) faults with grouped strikes in 3D models.

2.4. Salt body

RGM provides a functionality to insert one or multiple salt bodies into the random geological model. We use a four-step procedure to build randomly shaped salt bodies.

Step 1: Generate closed, randomized circular curves at control depths. We first generate closed, randomized circular curves to serve as the horizontal-slice profile of a salt body. We generate a random, periodic curve of N points based on random phases in the Fourier domain:

$$C_l = \Re \left\{ \mathcal{F}^{-1} \left[\left(\frac{1}{(\varepsilon N)^2} + k^2 \right)^{-1/2} \exp(i r_l) \exp(-\omega k^2) \right] \right\}, \tag{47}$$

where $\mathcal{F}^{-1}$ represents the inverse Fourier transform, $\Re$ represents the real part of complex values, $k = (-\pi/2, \pi/2]$ is the wavenumber vector, $r_l \in \mathcal{U}(0, 2\pi)$ is a random value sequence drawn from a uniform distribution with lower and upper bounds of 0 and 2π, respectively, ε is a parameter that controls the lower wavenumber content of the generated random values, which is set to 0.3 in RGM, ω is the smoothing parameter of the wavenumber domain Gaussian in the last term, which is set to 10 in RGM, and i is the unit imaginary number. The closed curve for serving as a shape-constraining perimeter at some depth is then computed as

$$P = R_0 + \left(\frac{C - \mu(C)}{\max(|C - \mu(C)|)} \right) \Delta R, \tag{48}$$

where R_0 is the base radius of the circular curve, and ΔR is the radius variation along the polar angle, and $\mu(C)$ represents the mean of C. The radius of this closed circular curve away from the center therefore falls within $[R_0 - \Delta R, R_0 + \Delta R]$.

We use P as the radii of the closed circular curve with an interval of 1° at this depth. We repeat the procedure with different random seeds for a total of N_c times, and obtain a total of N_c closed, randomized circular curves spanning N_z (the length of the vertical axis of the model). Figure 8 displays six examples of such curves defined by $R_0 = 10$ and $\Delta R = 5$.

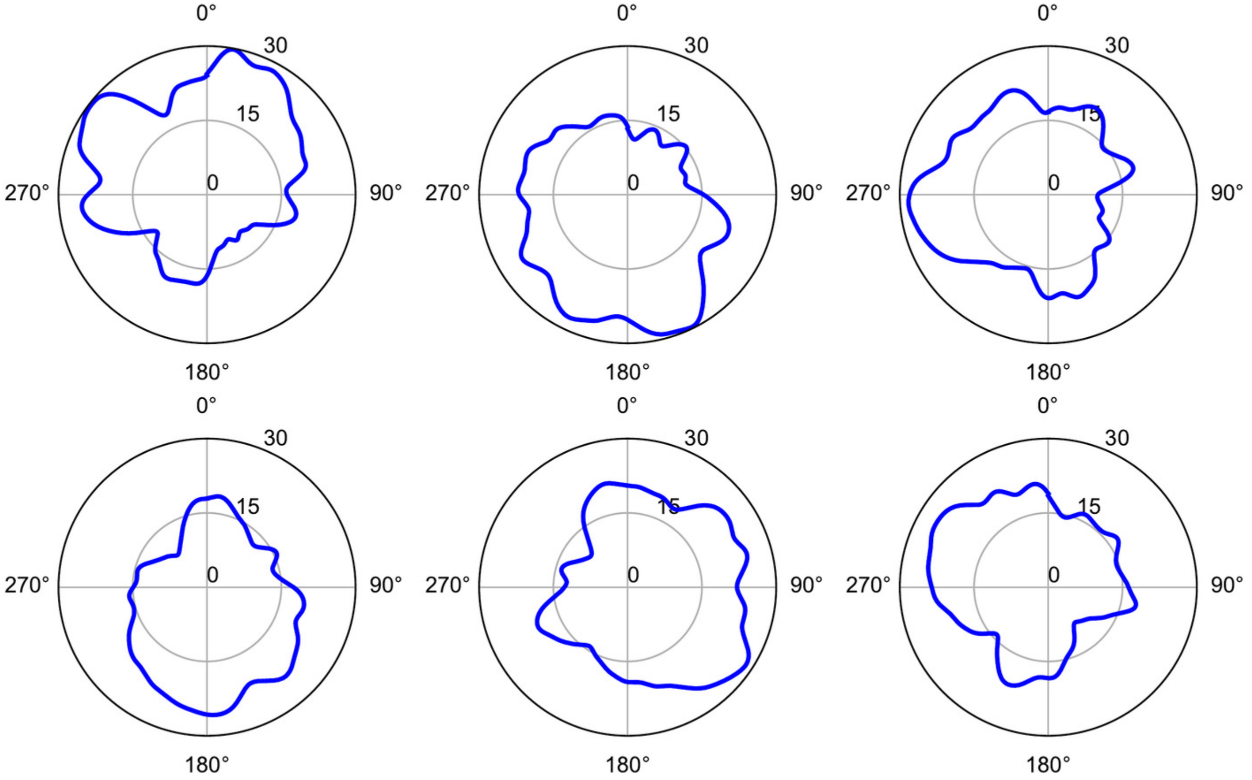

Figure 8: Six examples of random circular curves for creating a salt body.

Step 2: Connect the circular curves through monotonic spline curves. We connect the N_c through monotonic spline interpolation along the depth axis. In RGM, we achieve this step by interpolating the 2D array, say S, that holds the radii for the N_c curves from (360, N_c) to (360, N_z), where the interpolation along the second dimension (the depth axis) is achieved via the piecewise cubic Hermite interpolating polynomial (PCHIP) interpolation (Fritsch and Carlson, 1980). Using PCHIP interpolation yields more realistic salt profile than linear interpolation or simple cubic spline interpolation as it maintains monotonicity and smoothness simultaneously.

Step 3: Build the top surface. The last step of creating a salt body is adding a random top surface for the salt body. In RGM, we achieve this step by defining a 2D multi-octave Perlin noise, linearly transforming it the value range of $[0, \Delta h_{\text{salt}}]$ where Δh_{salt} is the maximum height variation of the salts' top surfaces defined by the user, and finally intersecting the PCHIP-interpolated salt body using this top surface at some random depth within a predefined depth range $[z_{\text{salt,min}}, z_{\text{salt,max}}]$.

Step 4: We then fill the salt body using a constant value corresponding to the salt body, say, v_{salt}. We achieve this step by checking if a grid point (x, y) falls within the shape-controlling curves at every depth. In specific, assuming the center of the horizontal slice of a salt body is $(x_s(z), y_s(z))$ at the depth of z, then a point (x, y) at the same depth corresponds to the radius with an index of

$$l = \left[\arctan\left(\frac{x - x_s(z)}{y - y_s(z)}\right)\right] + 181, \tag{49}$$

where $[x]$ represents rounding x to the nearest integer. Since the distance of the grid point to the center is $d = \sqrt{(x - x_s(z))^2 + (y - y_s(z))^2}$, then if $d \leq S(l, z)$ and $z \geq z_{\mathrm{top}}$, the point falls within the created salt body (i.e., is in the circular randomized curve at z). We repeat the procedure for all the grid points, then complete the creation of a randomized salt body.

The steps for creating a salt can be represented by the workflow in Figure 9.

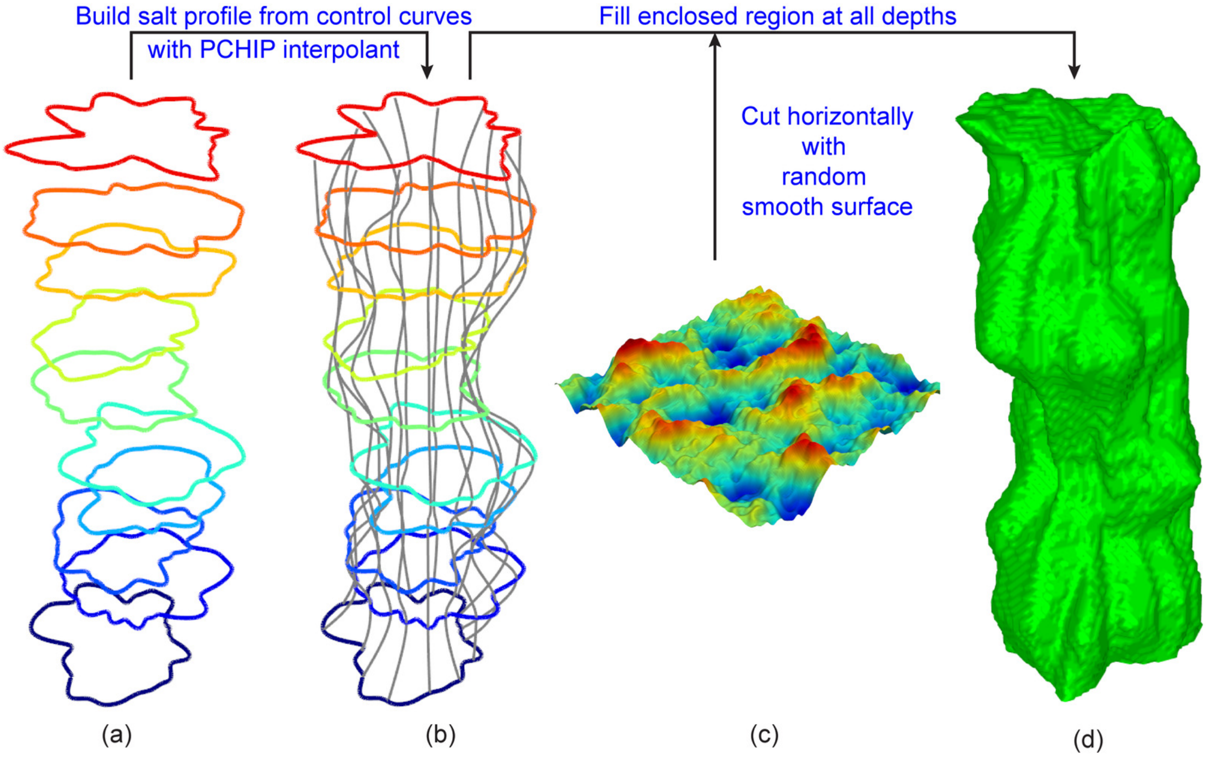

Figure 9: Workflow for generating a random salt body in RGM: (a) Define sparse control random circular curves at different depths. (b) Interpolate along the depth axis with the PCHIP method to construct a 3D salt body profile. (c) Create a random cutting surface and intersect it with the salt body as the top surface. Panel (d) shows the created random salt body.

2.5. Unconformity

RGM provides a functionality to insert one or multiple geological unconformities into the model, including disconformity (Figure 10a), paraconformity (Figure 10b), angular unconformity (Figures 10c and d), and nonconformity (Figures 10e and f). We use a three-step procedure to build a random geological model with N_u unconformities.

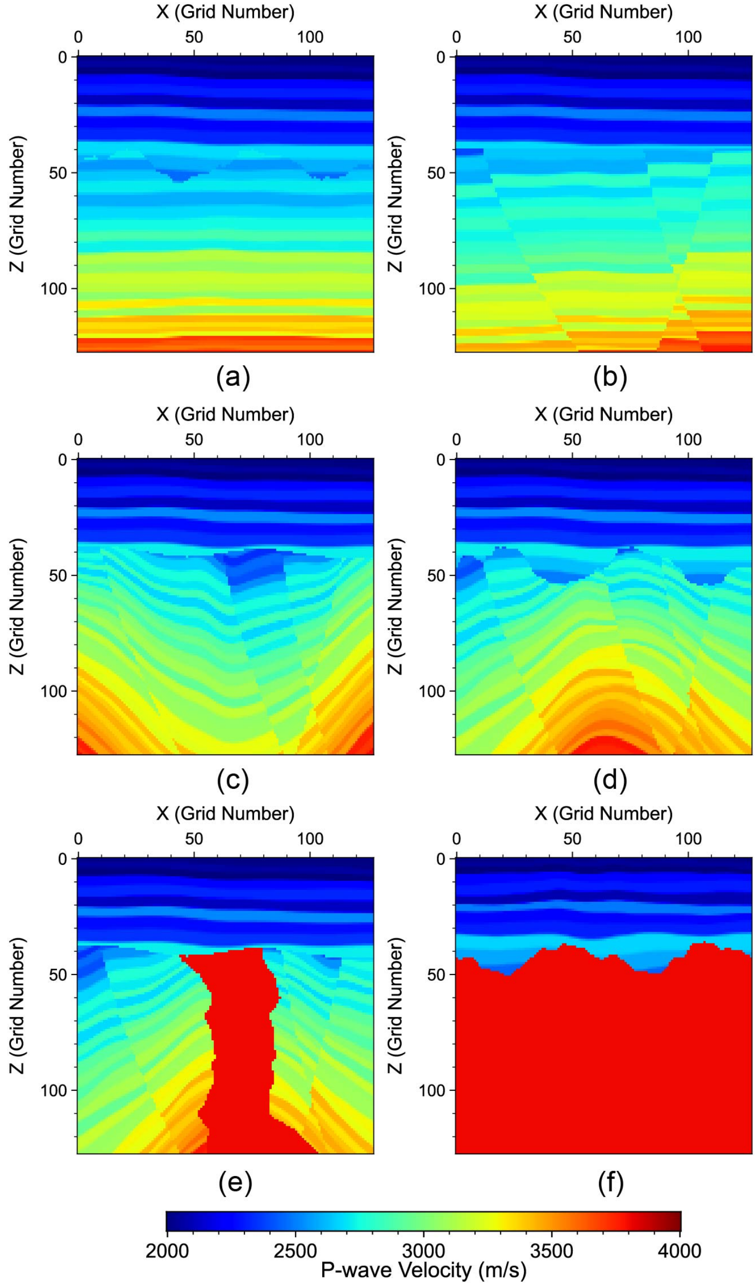

Figure 10: Different types of geological unconformities that can be simulated with RGM: (a) disconformity, (b) paraconformity, (c-d) angular unconformity, (e-f) nonconformity. Panel (e) also represents the case of mixed angular unconformity and nonconformity. In panels (e-f), the red color represents a salt body or magmatic intrusion.

Step 1: Generating $N_u + 1$ random geological models: To mimic realistic unconformity geology, the top N_u

geological models are free of faults, while the bottom-most geological model (i.e., the $N_u + 1$-th model at the bottom) contains or does not contain faults. The top N_u random geological models generally have smaller lateral variations of reflectors and thickness variations of layers.

Step 2: Generating N_u unconformities: We generate a total of N_u random surfaces using using the methods describe in the first section. Each unconformity interface/surface uses a different random seed for random value generation, which ensures that the unconformities have distinct shapes. RGM provides a number of tunable options to control the maximum depth, the maximum height (i.e., horizontal variation), as well as the shapes of unconformities.

Step 3: Merging: We merge the $N_u + 1$ geological models into the final geological model at each of the N_u unconformal surfaces. We use different merging methods for merging different models. For medium property models, starting from the bottom-most, we remove the medium property models for the grid points above the N_u-th unconformity surface, and replace them with the N_u-the model. We repeat this procedure until the top-most unconformity surface. For RGT, we first determine the minimum value $R_{\text{below,min}}$ of RGT below an unconformity interface and the maximum value $R_{\text{above,max}}$ of RGT above the unconformity interface, then RGT above the interface is adjusted by

$$T'_{\text{above}} = T_{\text{above}} - T_{\text{above,max}} + T_{\text{below,min}}, \tag{50}$$

$$T = T'_{\text{above}}(\mathbf{x}_{\text{above}}) + T_{\text{below}}(\mathbf{x}_{\text{below}}), \tag{51}$$

where $\mathbf{x}_{\text{above}}$ and $\mathbf{x}_{\text{below}}$ represent the grid points above and below the unconformity surface, respectively. After all the mergings, we linearly transform the entire RGT volume to the value range of $[0, 1]$:

$$T' = \frac{T - T_{\min}}{T_{\max} - T_{\min}}. \tag{52}$$

2.6. Seismic image

At each depth z_i, we compute the reflection coefficient associated with V_p and ρ as

$$R_{pp}(z_i) = \frac{V_p(z_{i+1})\rho(z_{i+1}) - V_p(z_i)\rho(z_i)}{V_p(z_{i+1})\rho(z_{i+1}) + V_p(z_i)\rho(z_i)}, \tag{53}$$

for $i = 1, 2, \cdots, N_l$. Repeating this procedure for all grid points creates a seismic image associated with the generated random geological model. RGM can also generate synthetic elastic migration images including PS, SP, and SS images in addition to the PP image using the method described by our previous work Gao and Chen (2025). For simplicity, we do not repeat the equations and procedure here.

Assume the spatial representation of the source wavelet is $w(z)$ (here, z is analogous to time t in the usual definition of a source time function), then the spatial point spread function (PSF) is defined as

$$w(x, y, z) = w(z - z_c) \exp\left(-\frac{(z - z_c)^2}{2\sigma_z^2}\right) \exp\left(-\frac{(y - y_c)^2}{2\sigma_y^2}\right) \exp\left(-\frac{(x - x_c)^2}{2\sigma_x^2}\right), \tag{54}$$

where (x_c, y_c, z_c) is the center of the gridded geological model, and $(\sigma_x, \sigma_y, \sigma_z)$ are the standard deviations of the multi-dimensional Gaussian controlling the spatial spreads of the source wavelet. Because the wavelet is defined along z only, a large σ_x (or σ_y) will result in more smeared image. The default values in RGM are $(\sigma_x, \sigma_y, \sigma_z) = (2.5, 2.5, 5)$.

We then obtain a seismic image as

$$I(x, y, z) = \Re\left\{\mathcal{F}^{-1}\left[\mathcal{F}[R(x, y, z)]\mathcal{F}[w(x, y, z)]\right]\right\}, \tag{55}$$

where $\mathcal{F}$ and $\mathcal{F}^{-1}$ represent the Fourier and inverse Fourier transforms, respectively.

2.7. Workflow

We use Figure 11 to summarize RGM's workflow to generate random medium parameter models, RGT volumes, and seismic migration images, with or without unconformity surfaces, salt bodies, and faults. Figure 11a displays the procedure of generating a faulted medium parameter model and a RGM volume, while Figures 11b and c display the process of generating a model containing one or multiple unconformities and salt bodies, respectively. Note that for the elastic model case, RGM computes four migration images (PP, PS, SP, and SS) as discussed in the previous subsection. In addition, both unconformity surfaces and salt bodies can exist in a generated random model. In this case, one can choose whether the salt bodies penetrate through the unconformity surfaces or not in RGM to improve reality.

3. Implementation and scalability

We implement the above methods using modern object-oriented Fortran ($\geq$ Fortran 2003). We parallelize computation-heavy loops (e.g., moving grid points for faulting) with OpenMP.

We perform scalability tests for both 2D and 3D cases. We set the number of grid points to be $N_x = N_y = N_z = 50, 100, 150, 200, 250, 300, 350, 400, 450$ or 500 in 2D or 3D. For each of the ten cases in 2D or 3D, we vary the number of faults from 1 to 20, as the number of faults directly affect the computation time in RGM. We run all the generations on a Intel Xeon Gold 6248R central processing unit (CPU) with 48 cores. Figure 12 displays the wall-clock time for the 2D and 3D cases. In 2D, because of the short computation time needed to accomplish a model generation as well as the randomness of fault geometric properties, there appear some sharp changes in CPU times over different numbers of faults as well as different numbers of grid points. In 3D, at least for small models, the generation is very efficient. For example, the CPU times for generating a model with dimensions of $N_z \times N_y \times N_x = 150 \times 150 \times 150$ range from

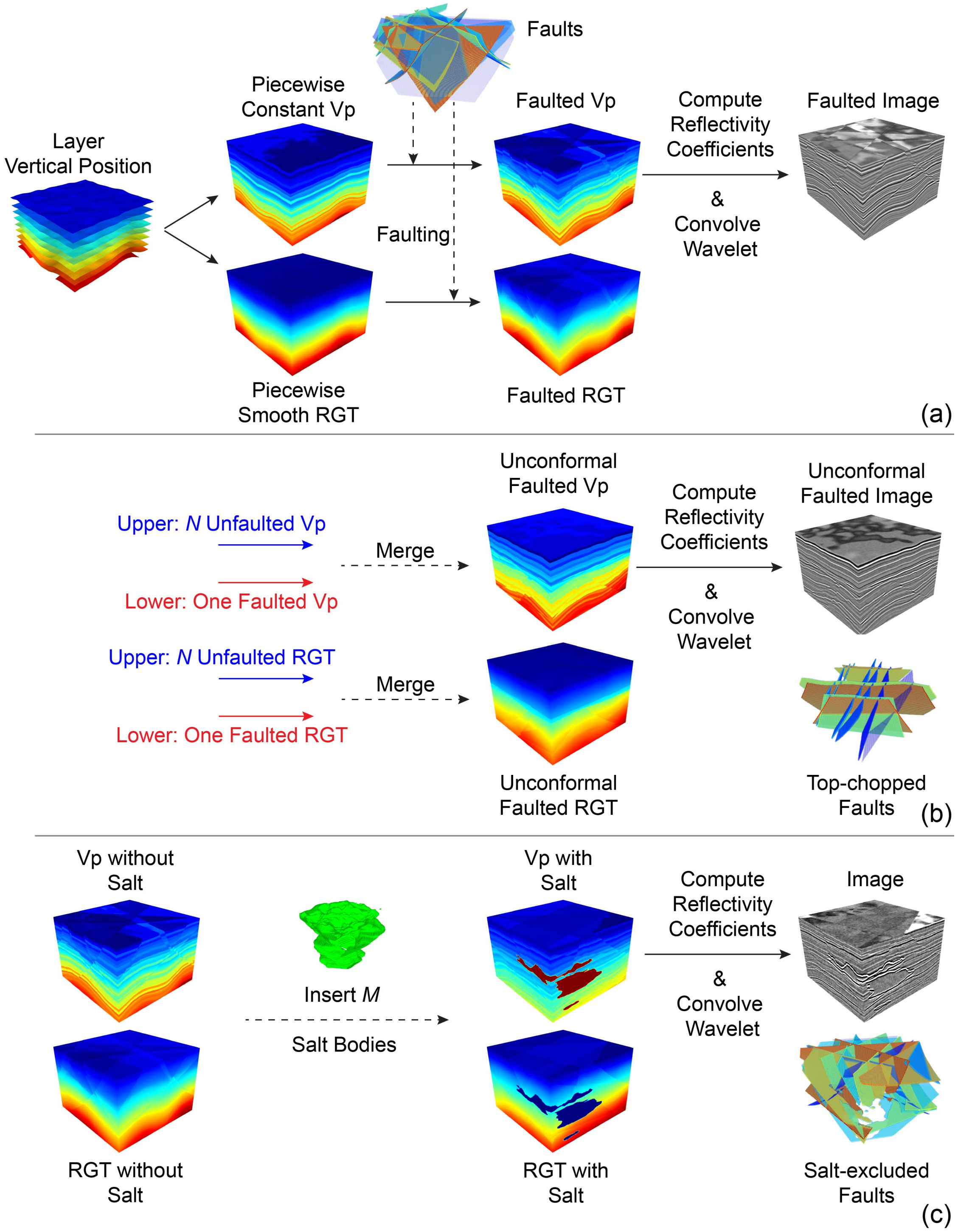

Figure 11: Workflows for generating random models with RGM. Panel (a) is the procedure for generating faulted models starting from a series of layer vertical positions. Panel (b) shows how RGM generates an unconformal model, while panel (c) shows how RGM generates a model with one or multiple salt bodies. The procedures for inserting faults, unconformity surfaces, and salt bodies have been described in the previous subsections.

2.62 s (one fault) to 6.32 s (20 faults). For larger models ($N = 500$), the times vary from 93 s to 148 s.

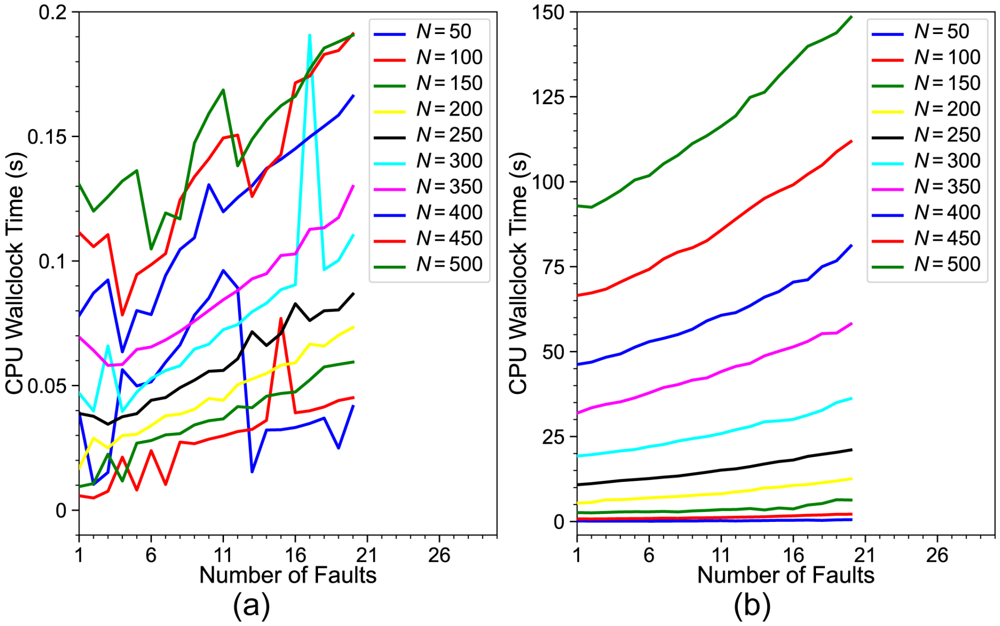

Figure 12: Comparisons of wall-clock CPU times for generating random geological models in (a) 2D and (b) 3D, respectively. N is the number of grid points along each axis.

4. Examples

Figure 13 display six examples of unfaulted random P-wave velocity models generated by RGM in Figures 13a-c (2D) and Figures 13d-f (3D), respectively. The density models are simply built based on the Gardner's rule. Horizontal smoothness of the layers varies from low (Figures 13c, e, and f) to high (Figures 13a, b, and d). Figure 14 displays the RGTs corresponding to the medium property models in Figure 13. Figure 15 displays the seismic images corresponding to the medium property models in Figure 13.

Next, we display several examples of faults and faulted geological models. Figure 16 displays six examples of geological faults in the 2D and 3D cases. Faults in Figures 16a and d are mostly straight or with only small dip variations in depth, whereas the other four examples display listric faults with decaying dips in depth. We use different colors in these plots to represent fault indices (ranging from 1 to the maximum number of faults in a model). This is useful for instance segmentation where an ML model identifies and segments faults individually.

Further, we display the fault dip and fault strike models generated by RGM in Figure 17 corresponding to the fault index models displayed in Figure 16. The faults in Figure 17 are colored by dip or strike angles. These models can be used to train multitask ML model for inferring geometric properties of faults directly from seismic images on a pixel level (Gao, 2024).

Applying the faults displayed in Figure 16 and Figure 17 to unfaulted geological models yields the faulted V_p

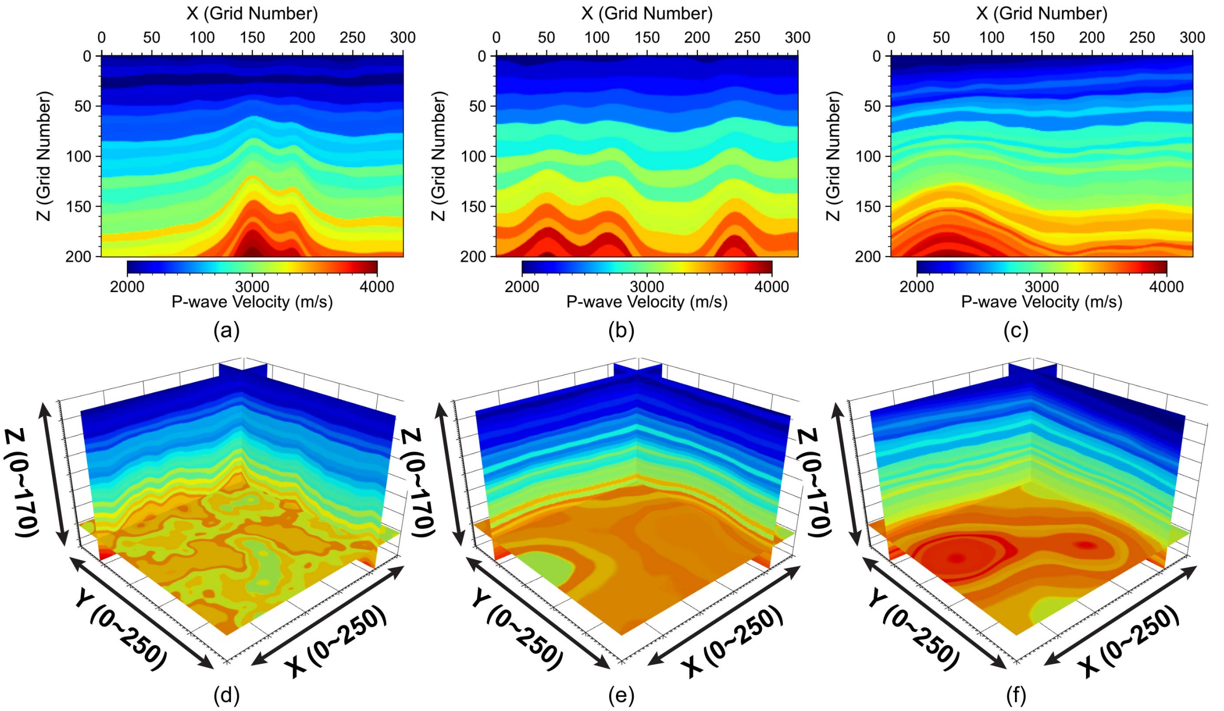

Figure 13: Examples of random geological models generated by RGM: (a-c) 2D and (d-f) 3D unfaulted medium property models (V_p). In this figure and figures thereinafter, if both 2D plots and 3D plots appear, the 3D plots share the same color scale with the 2D plots.

models displayed in Figure 18. By randomizing the fault displacement associated with the faults in RGM, we obtain normal faults (positive fault displacement) or reverse faults (negative fault displacement), resulting in close resemblance to realistic complex fault network. Figure 19 displays the RGTs corresponding to the velocity models in Figure 18. The most notable feature of faulted RGTs is the sharp discontinuity in the horizontal directions compared with in the depth direction. Figure 20 displays the corresponding seismic images, where we observe clear lateral discontinuities of reflectors caused by the faults.

It is worth noting that with RGM, by setting the rake angle of faults to $\varphi = 0$ or π, the user can generate strike-slip faults (i.e., faults with displacement mostly in the horizontal directions), a unique type of fault that can only exist in the 3D scenario. Depending on the structure, strike-slip may not generate notable vertical fault displacements that can be captured by imaging algorithms. Figure 21 displays such an example of seismic image with two strike slip faults, where the red arrows point to the faults that generate notable horizontal displacements but not obvious vertical displacements (pointed by the yellow arrows). Similarly, by setting $\varphi = \pi/2$, the user can obtain normal or reverse faults without horizontal fault displacements.

Next, Figure 22 displays six examples of random geological models with salt bodies in 2D and 3D. We set different sizes, shapes, as well heights for these salt bodies. In the 3D models displayed Figures 22d-f, we purposely use large

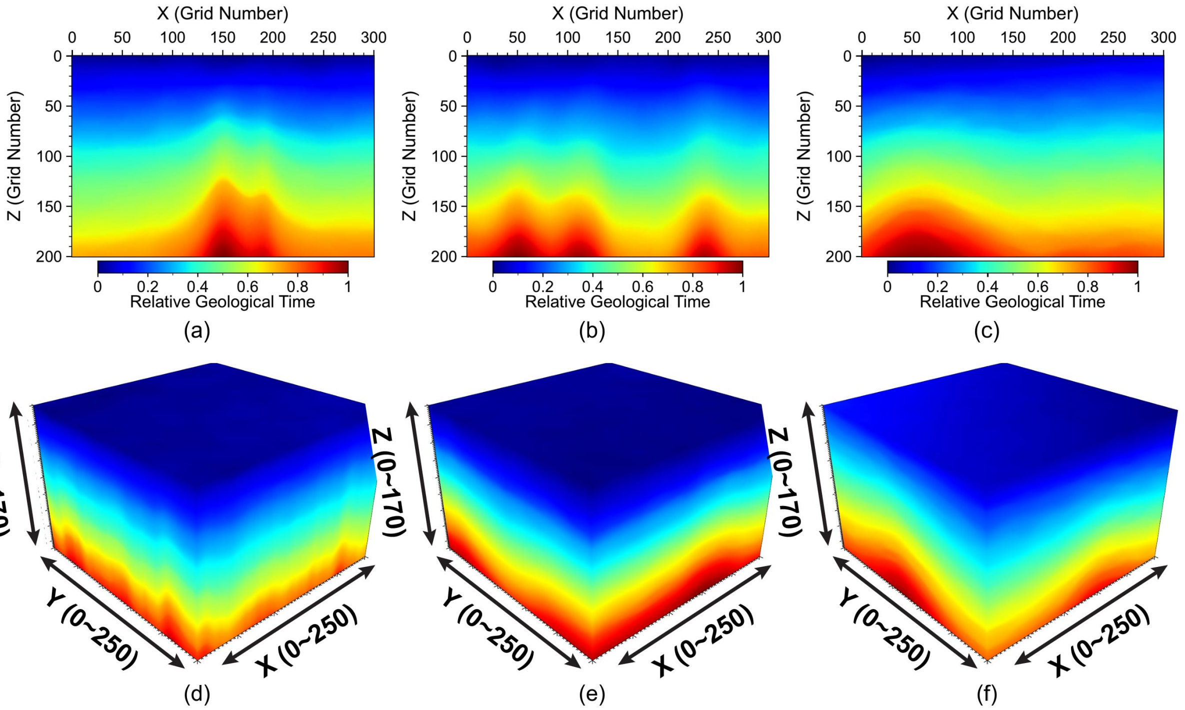

Figure 14: Examples of random geological models generated by RGM: (a-c) 2D and (d-f) 3D RGT models corresponding to the V_p models in Figure 13.

diameter variations for each of the salt bodies. This yields mushroom-like top for the synthetic salt bodies, mimicking post-intrusion spreading along the layers (Hudec and Jackson, 2007). Figure 23 displays the seismic images associated with the models in Figure 22.

We also generate geological models with unconformities using the method described in the *Methodology* section. Figure 24 displays six examples of velocity models that contain one or two unconformities. Figures 24a and d display two cases with relatively high-amplitude unconformities, while the other four models have relatively smooth unconformity surfaces. Figures 24a, c, and d display the cases of angular unconformity, where the unconformity interfaces cut through earlier deformed sedimentary layers and form notable angular discontinuity.

Figure 25 displays the RGTs corresponding to the models in Figure 24. As described in the *Methodology*, in this case the RGT may form clear discontinuity. This is because an unconformity in RGM means complete removal of the points above the unconformity and that the RGT resumes from the youngest time of the part below the unconformity. Depending on the amplitude of an unconformity, this time discontinuity could be notable.

Figure 26 displays the seismic images associated with the unconformal medium parameter models in Figure 24. It could be seen that the reflector image associated with an unconformity is generally non-zero. Correctly identifying these special reflectors on a seismic image can help identify unconformity and therefore better understand the geological

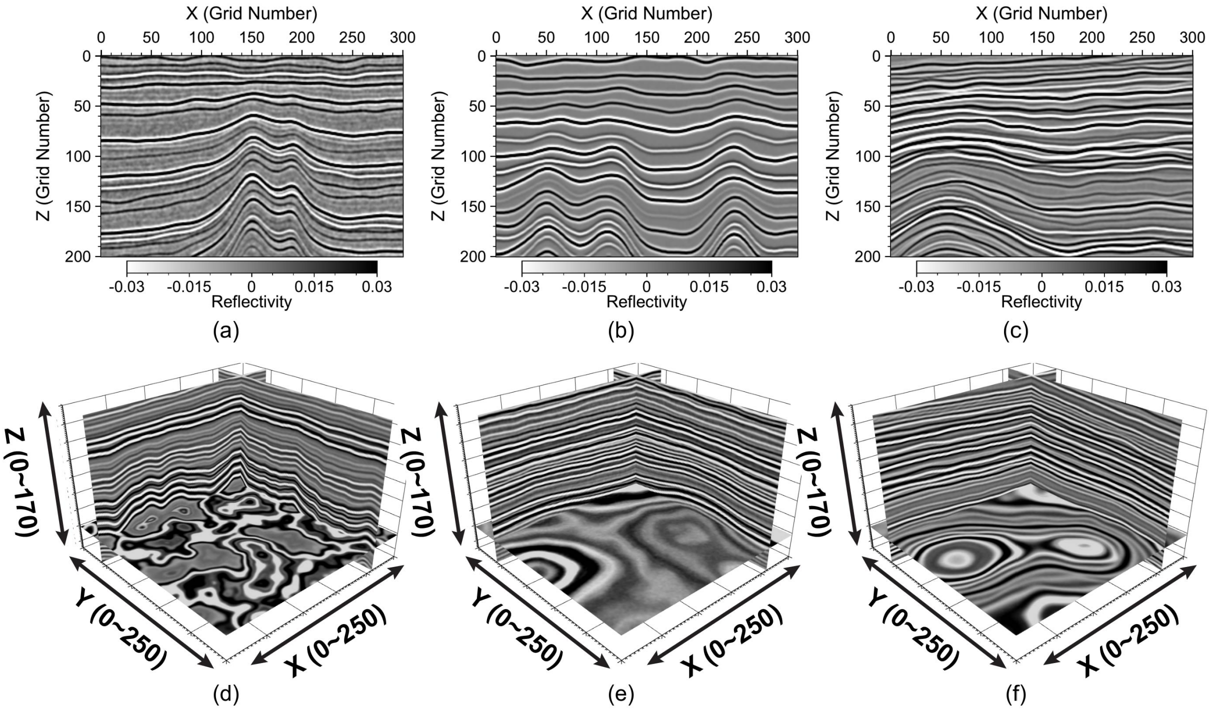

Figure 15: Examples of random geological models generated by RGM: (a-c) 2D and (d-f) 3D seismic images corresponding to the V_p models in Figure 13.

evolution.

Figure 27 display the fault dip and strike angles associated with the velocity models and seismic images displayed in Figures 24 and 26. We described in the methodology, in RGM, we assume unconformity (and its later sedimentation) are the last geological events when salt does not present, therefore the unconformity interface or surface cut through faults and sedimentation earlier than the unconformity event; that is, above the earliest unconformity surface, there is no fault. This is consistent with the truncated faults displayed in Figure 27. In Figures 17b, d, and g, we insert one or multiple salt bodies into the geological models. Therefore, the faults inside the salt bodies are removed, appearing as "broken" lines/curves or "holed" surfaces.

As faulted images and faults are widely used as input data and labels for training ML models, we display another 16 examples of seismic images and the corresponding fault index labels in Figure 28. These examples cover different numbers and types of faults, where some of them contain unconformity.

Lastly, we display some 2D elastic models and migration images generated by RGM in Figure 29. Figures 29a and b display the V_p and V_s models generated by RGM. There are multiple faults as well as an unconformity interface in the model. Figures 29c-f display the PP, PS, SP, and SS images generated by RGM, overlain on the the fault dip attribute. The four images show visually different vertical resolutions and amplitudes of reflection coefficients. The resolution of

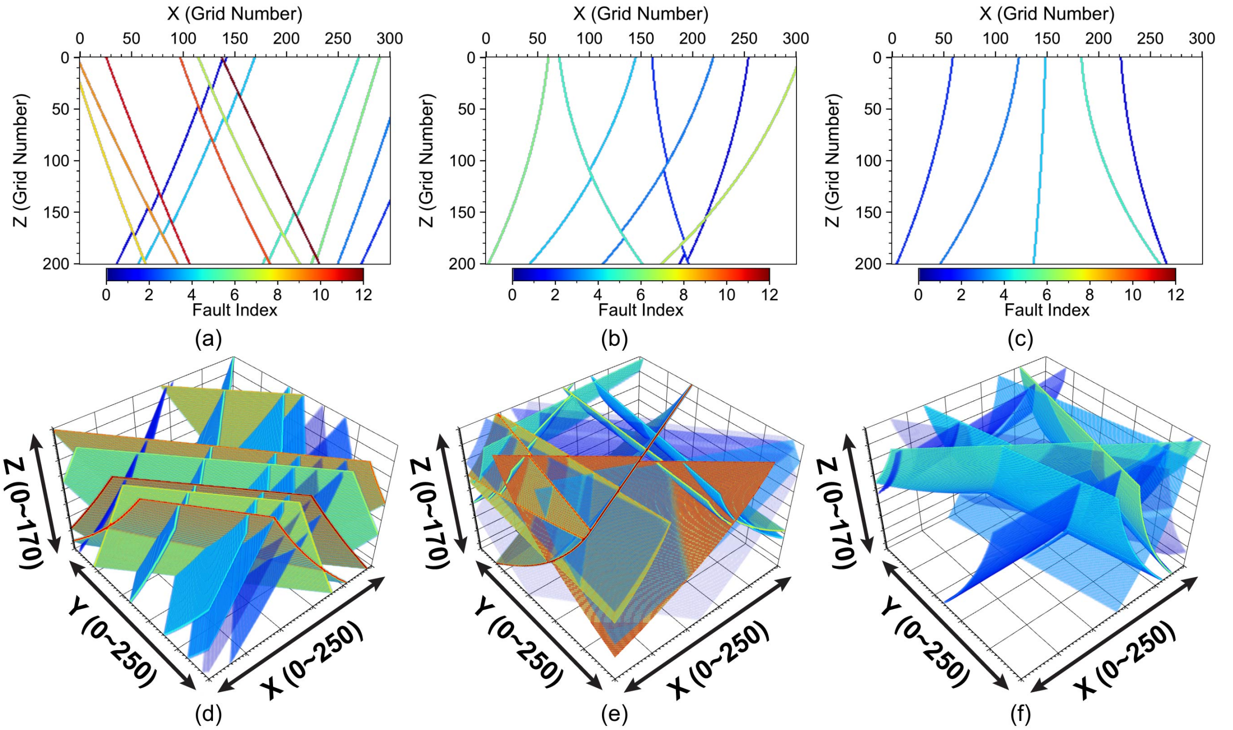

Figure 16: Examples of random geological models generated by RGM: (a-c) 2D and (d-f) 3D fault index models. Colors in these plots represent different faults.

the PP image is notably lower than that of the SS image, while the resolutions of PS and SP images are intermediate of the four images. In practice, depending on the source mechanism in a seismic survey, it is usually difficult to obtain four images with equal quality from multi-component seismic data. In such a case, one can choose to use of the synthetic elastic migration images generated by RGM for training ML models.

5. Discussions

We have described the methodology used in our RGM for generating high-fidelity random geological models, including medium parameter models, RGT volumes, seismic images, faults, fault attributes, salt bodies, and unconformities. We have also displayed examples of random geological models generated by RGM. It is worth mentioning some limitations of our current RGM implementation.

First, generation of medium property models in RGM is based completely on geometric methods (i.e., defining bounding surfaces and generating layers through interpolation). The resulting models mimic realistic geological models visually but not physically. Rigorous determination of layer structures may need solving static elasticity constitutive equations under tectonically meaningful boundary conditions, which can be computationally expensive. Furthermore, the current version of RGM cannot generate large deformation structures such as recumbent folds (Bastida et al., 2014).

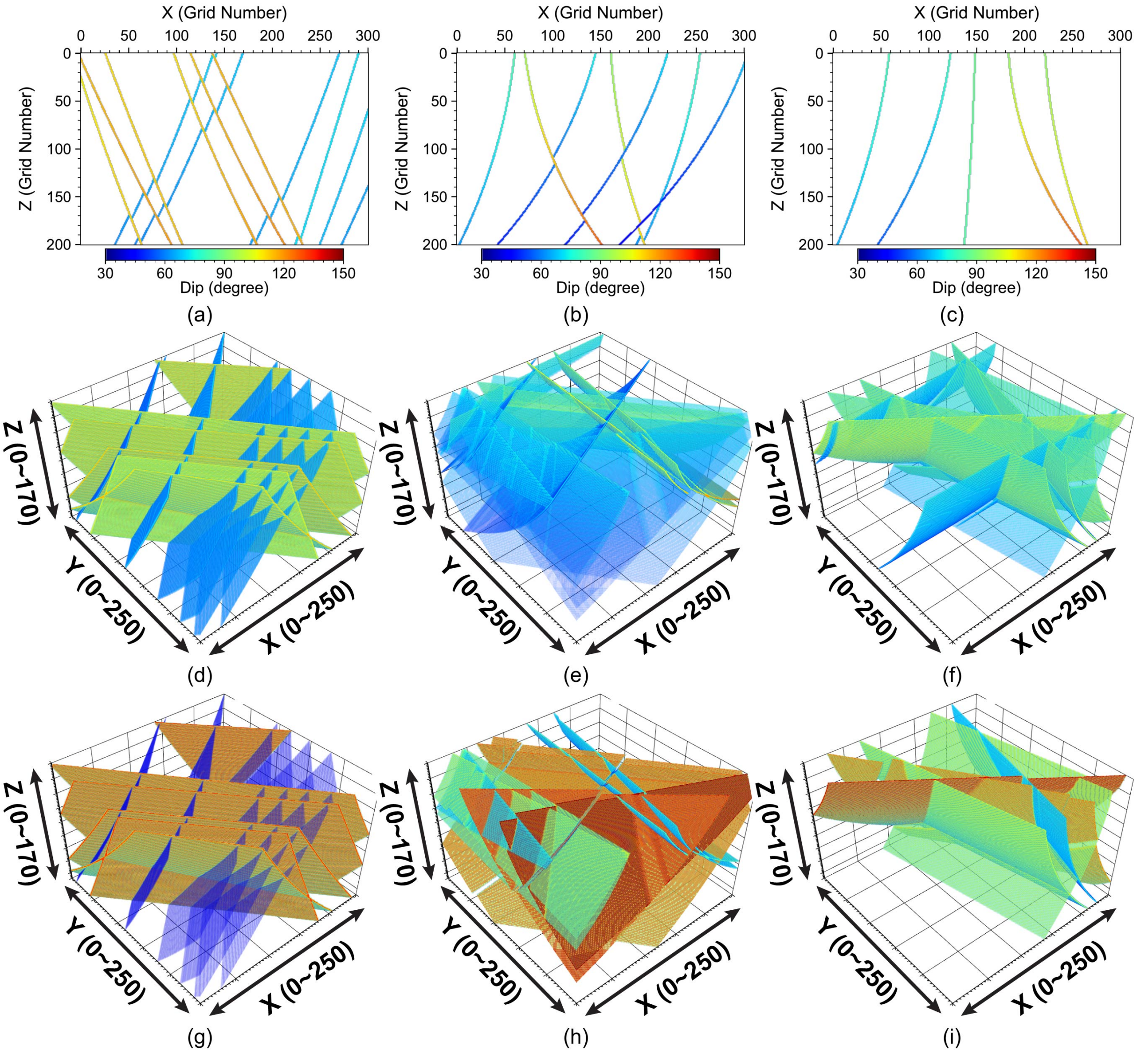

Figure 17: Examples of random geological models generated by RGM: (a-c) 2D fault dip attribute, (d-f) 3D fault dip attribute, and (g-i) 3D fault strike attribute. Both the 3D dips and strikes are displayed on a color scale of 50 to 130 degrees.

Future versions of RGM may provide functionalities to address these limitations.

Second, we adopt a simplified fault model in RGM. Realistic faults usually have non-constant fault displacement across the fault surface and away from the fault due to non-uniform sedimentary loading (Wu et al., 2020). In addition, in RGM we assume the strike angle of a fault is constant, while in practice the strike angle of a fault can slowly vary in space. However, properly implementing these features could become complicated when one intends to generate geometric attributes (dip, strike, displacement, and so on) of faults as labels in training ML models. Future versions of RGM may enable spatially varying displacement and strike angle for faults through adapting and modifying more

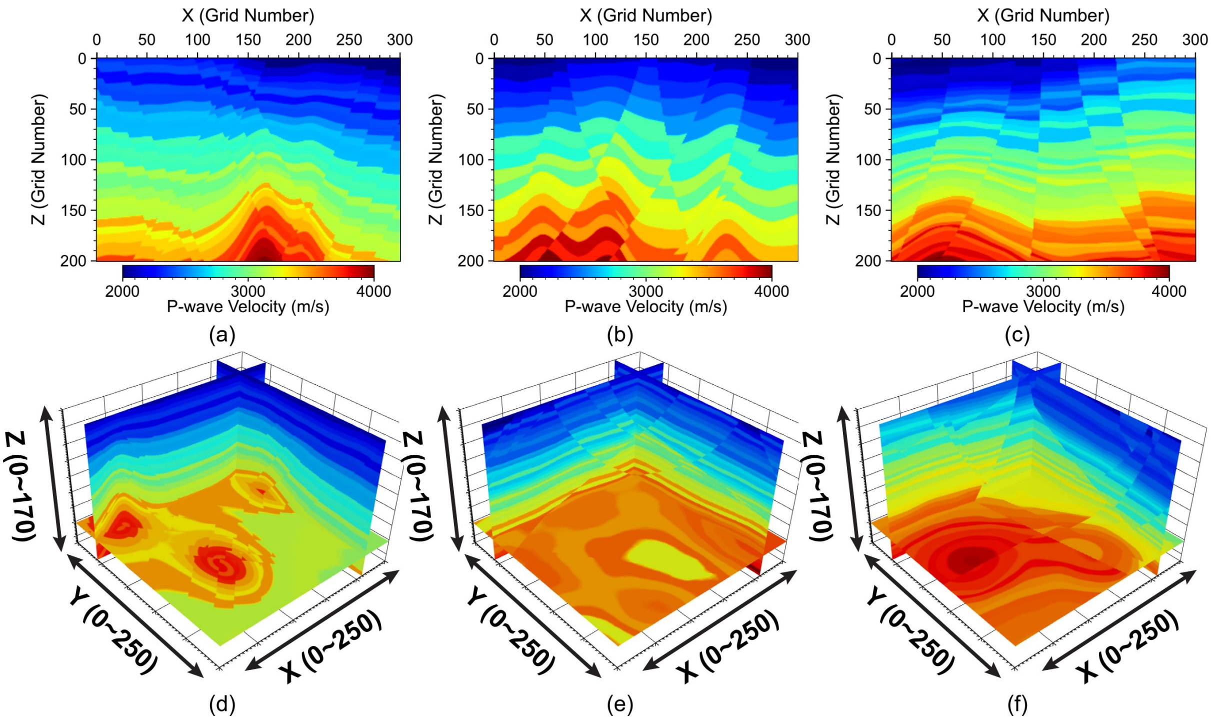

Figure 18: Examples of random geological models generated by RGM: (a-c) 2D and (d-f) 3D faulted V_p models.

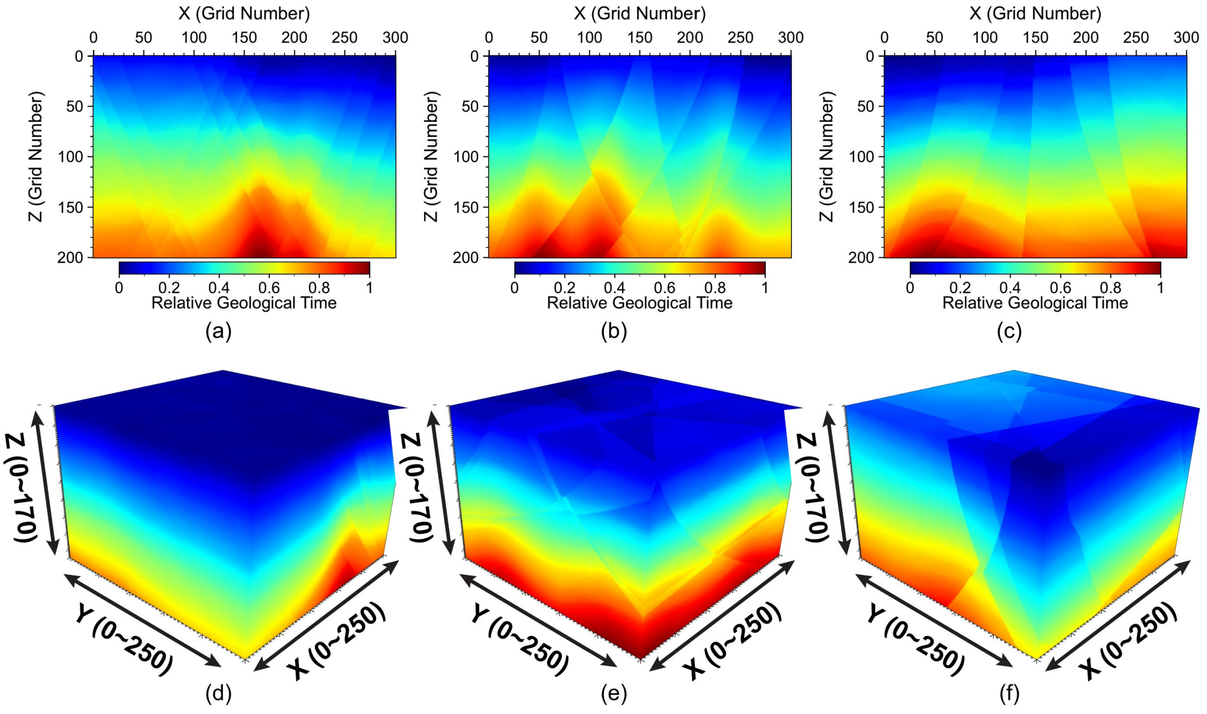

Figure 19: Examples of random geological models generated by RGM: (a-c) 2D and (d-f) 3D RGT models corresponding to the V_p models displayed in Figure 18.

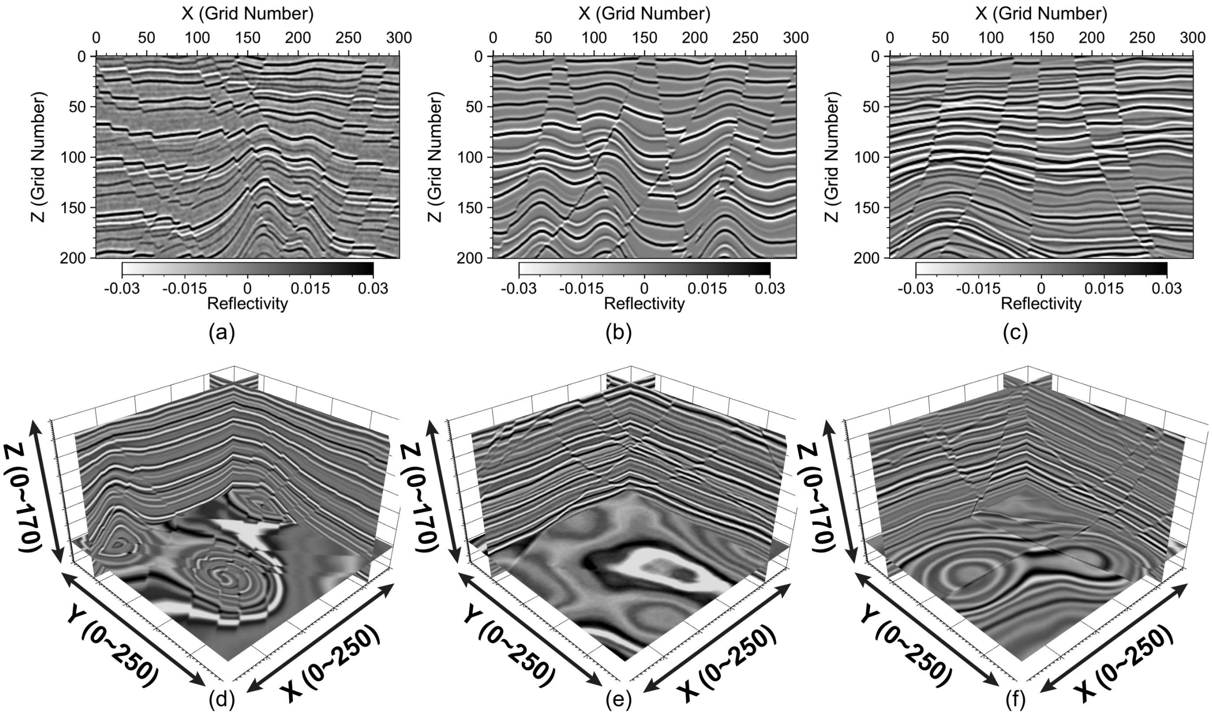

Figure 20: Examples of random geological models generated by RGM: (a-c) 2D and (d-f) 3D seismic images corresponding to the V_p models displayed in Figure 18.

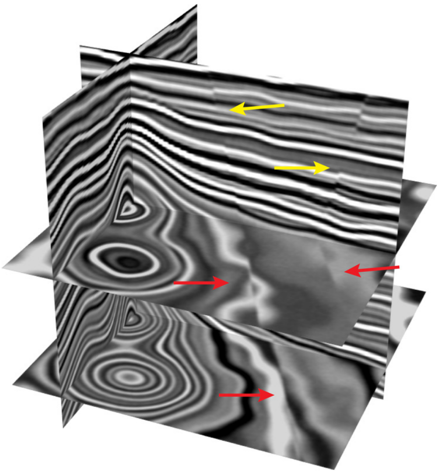

Figure 21: An example of 3D seismic image with two strike-slip faults. The faults cause displacements that are visible on the horizontal slice (denoted by the red arrows) while almost invisible on the vertical slices (denoted by the yellow arrows).

flexible methods (Georgsen et al., 2012; Wu et al., 2020).

Third, we adopt a simplified approach to inserting salt bodies into a geological model. We define bounding surfaces to control the shape of salt bodies. However, in practice, salt body intrusion can disturb subsurface stress and generate corresponding tectonic strain that deforms or breaks existing sedimentary layers, which should be properly considered

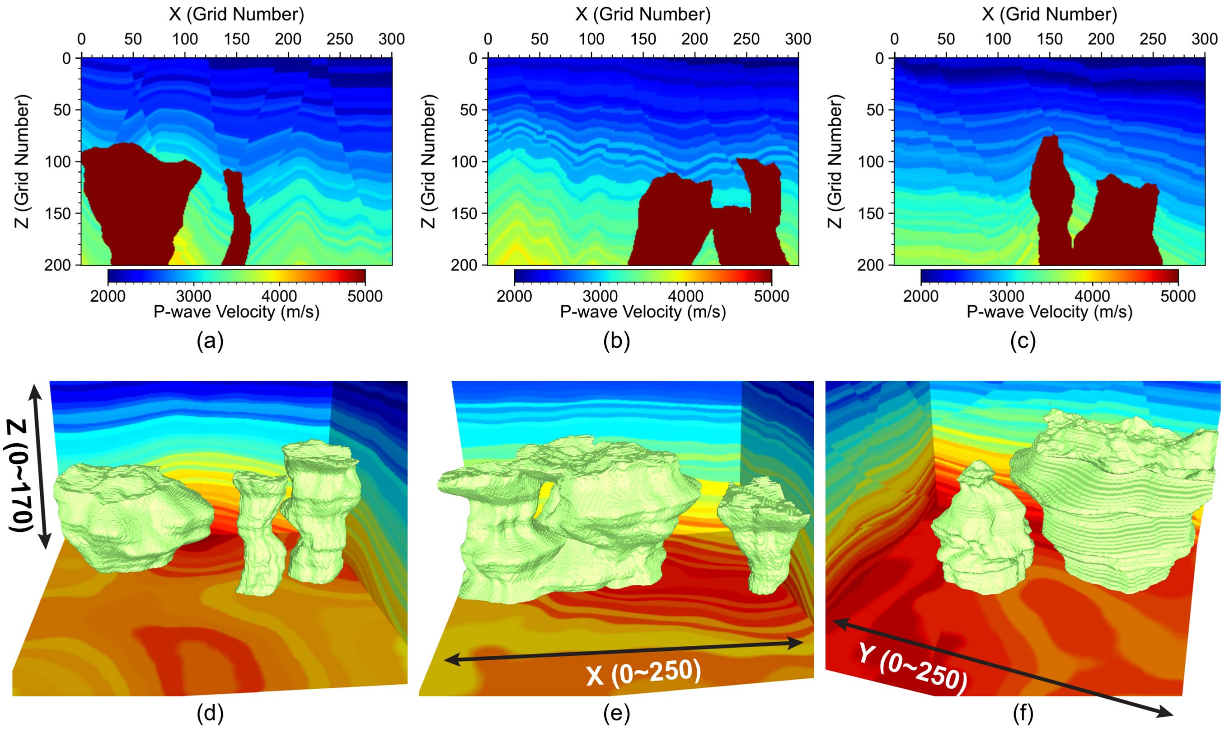

Figure 22: Examples of random geological models generated by RGM: (a-c) 2D and (d-f) 3D V_p models containing salt bodies.

in the geological modeling process as described by Hudec and Jackson (2007). Such accurate, physics-based simulation of salt bodies may need solving partial differential equations and is likely to be computationally expensive. Therefore, physics-based salt simulation is beyond the scope of this work.

6. Conclusions

We introduced RGM (Random Geological Modeling), an open-source package designed to efficiently generate synthetic geological models tailored for machine learning applications. RGM enables users to produce diverse and geologically plausible 2D and 3D models through a simple, customizable interface, offering fine control over statistical and structural parameters. The outputs include P- and S-wave velocity models, density models, synthetic seismic images, fault attributes (e.g., index, probability, dip, strike, rake, displacement), salt bodies, unconformities, and relative geological time fields. These outputs are well-suited for training ML models to recognize and interpret geological features from seismic data. We detailed the algorithms behind RGM's multi-randomization strategy and demonstrated its effectiveness through a series of 2D and 3D examples. The results show that RGM can generate high-fidelity, non-repetitive geological scenarios at scale. In future work, we aim to further enhance geological realism by incorporating more complex deformation processes and stratigraphic rules into the model generation workflow.

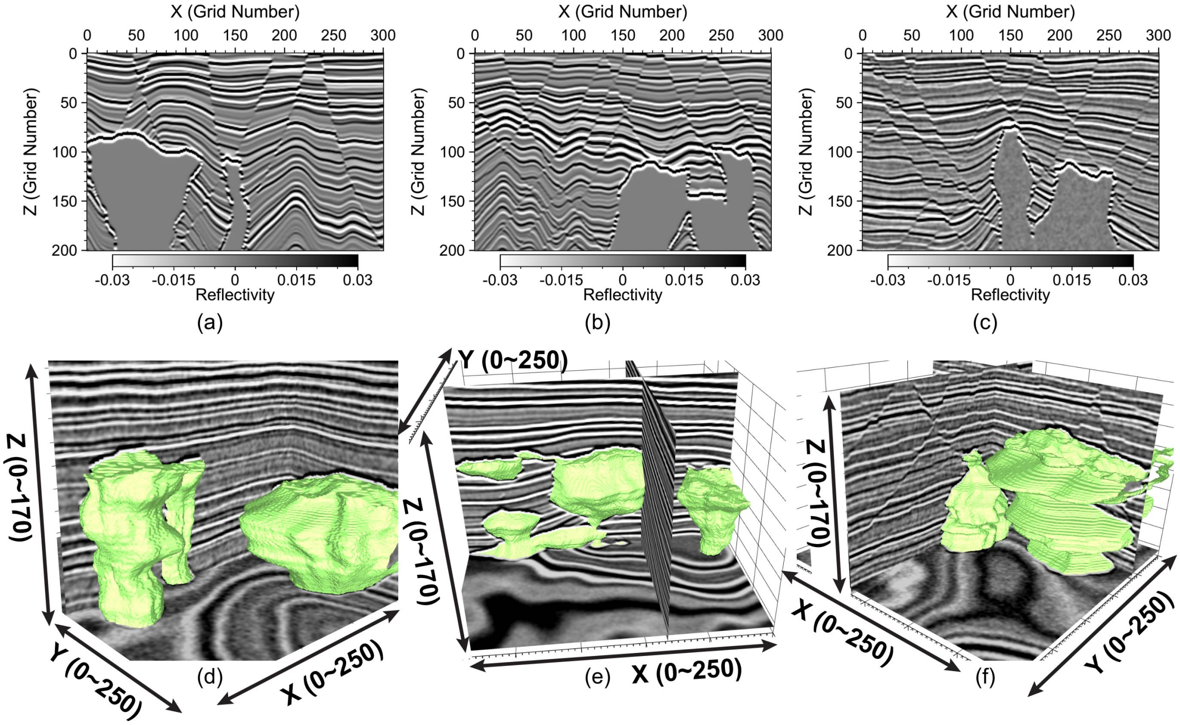

Figure 23: Examples of random geological models generated by RGM: (a-c) 2D and (d-f) 3D seismic images corresponding to the V_p models in Figure 22.

Code availability

The source codes associated with the method developed in this work and the scripts for reproducing the examples in the paper are available at `https://github.com/lanl/rgm`.

Acknowledgments

The work is supported by Los Alamos National Laboratory (LANL)'s Laboratory Directory Research and Development (LDRD) projects 20210528CR-CSE and 20240322ER. LANL is managed and operated by Triad National Security, LLC for the U.S. Department of Energy (DOE) National Nuclear Security Administration (NNSA) under contract No. 89233218CNA000001. The research used high-performance computing resources provided by LANL's Institutional Computing (IC) program. The codes associated with the paper are approved for public release under BSD 3-Clause license by LANL's Feynman Center for Innovation (FCI) under record number O4778. The work is approved for public release under LA-UR-25-27984.

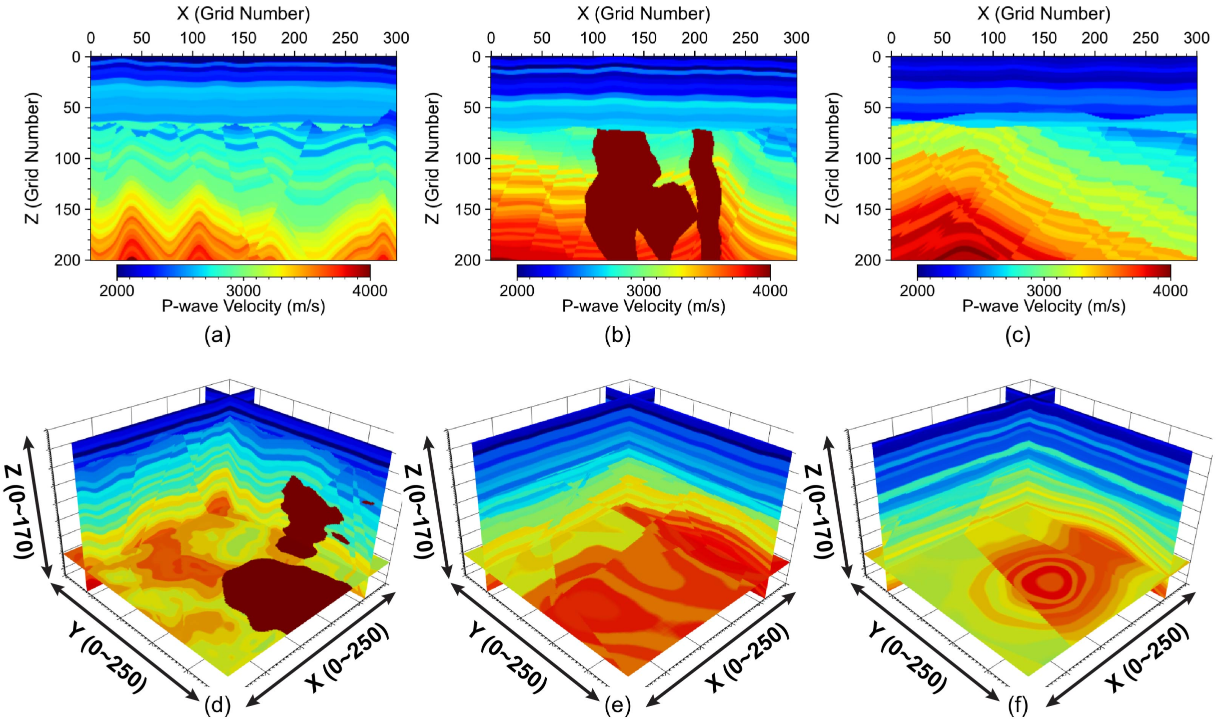

Figure 24: Examples of random geological models generated by RGM: (a-c) 2D and (d-f) 3D V_p models containing one or multiple unconformity surfaces.

References

Bastida, F., J. Aller, F. J. Fernández, R. J. Lisle, N. C. Bobillo-Ares, and O. Menéndez, 2014, Recumbent folds: Key structural elements in orogenic belts: Earth-Science Reviews, **135**, 162–183, doi: `10.1016/j.earscirev.2014.05.002`.

Bi, Z., X. Wu, Z. Geng, and H. Li, 2021, Deep relative geologic time: A deep learning method for simultaneously interpreting 3-D seismic horizons and faults: Journal of Geophysical Research: Solid Earth, **126**, no. 9, 10.1029/2021JB021882, doi: `10.1029/2021JB021882`.

Calcagno, P., J. Chilès, G. Courrioux, and A. Guillen, 2008, Geological modelling from field data and geological knowledge: Part I. Modelling method coupling 3D potential-field interpolation and geological rules: Physics of the Earth and Planetary Interiors, **171**, no. 1, 147–157, doi: `10.1016/j.pepi.2008.06.013`.

Cardozo, N., P. Røe, H. H. Soleng, N. Fredman, J. Tveranger, and S. Schueller, 2008, A methodology for efficiently populating faulted corner point grids with strain: Petroleum Geoscience, **14**, no. 2, 205–216, doi: `10.1144/1354-079308-738`.

Caumon, G., P. Collon-Drouaillet, C. Le Carlier de Veslud, S. Viseur, and J. Sausse, 2009, Surface-based 3D modeling of geological structures: Mathematical Geosciences, **41**, no. 8, 927–945, doi: `10.1007/s11004-009-9244-2`.

de la Varga, M., A. Schaaf, and F. Wellmann, 2019, GemPy 1.0: open-source stochastic geological modeling and inversion: Geoscientific Model Development, **12**, no. 1, 1–32, doi: `10.5194/gmd-12-1-2019`.

de la Varga, M., and J. F. Wellmann, 2016, Structural geologic modeling as an inference problem: A bayesian perspective: Interpretation, **4**, no. 3, SM1–SM16, doi: `10.1190/INT-2015-0188.1`.

Deng, J., W. Dong, R. Socher, L.-J. Li, K. Li, and L. Fei-Fei, 2009, Imagenet: A large-scale hierarchical image database: Proceedings of IEEE

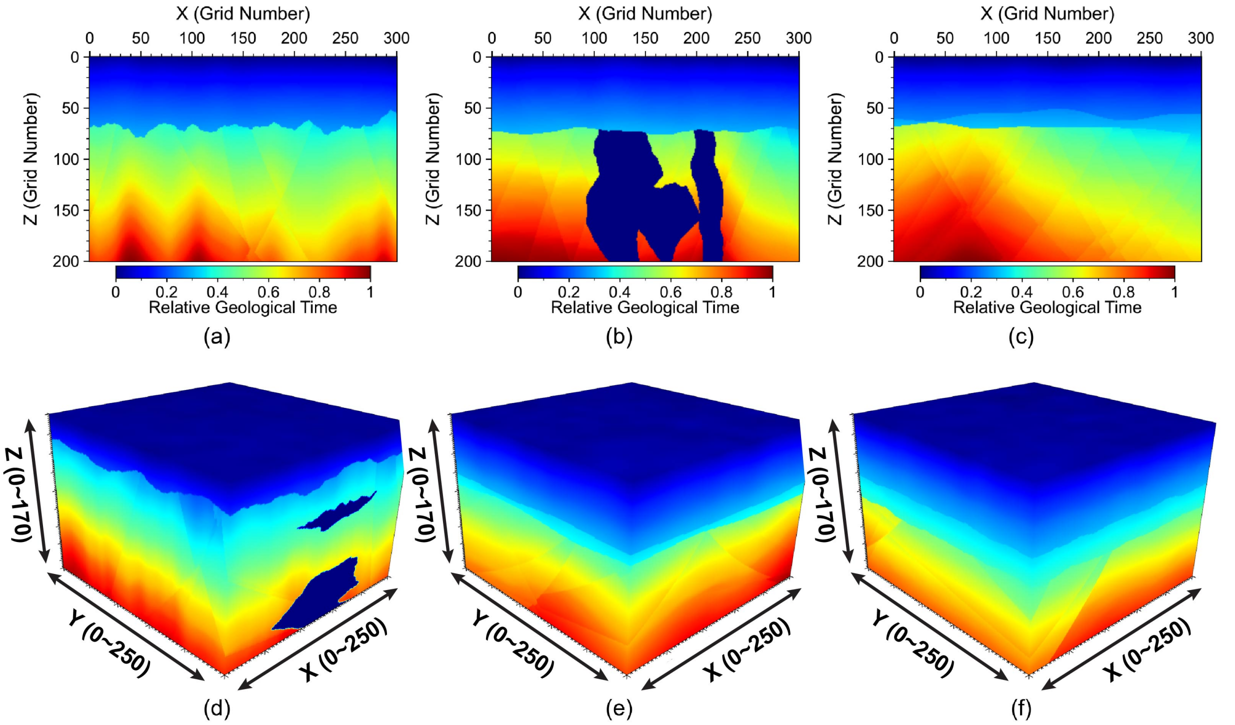

Figure 25: Examples of random geological models generated by RGM: (a-c) 2D and (d-f) 3D RGT images corresponding to the velocity models in Figure 24.

Conference on Computer Vision and Pattern Recognition, 248–255, doi: 10.1109/CVPR.2009.5206848.

Di, H., Z. Li, H. Maniar, and A. Abubakar, 2020, Seismic stratigraphy interpretation by deep convolutional neural networks: A semisupervised workflow: Geophysics, **85**, no. 4, WA77–WA86, doi: 10.1190/geo2019-0433.1.

Di, H., M. Shafiq, and G. AlRegib, 2018, Patch-level MLP classification for improved fault detection: SEG Technical Program Expanded Abstracts, 2211–2215, doi: 10.1190/segam2018-2996921.1.

Etherington, T. R., 2022, Perlin noise as a hierarchical neutral landscape model: Web Ecology, **22**, no. 1, 1–6, doi: 10.5194/we-22-1-2022.

Fritsch, F. N., and R. E. Carlson, 1980, Monotone piecewise cubic interpolation: SIAM Journal on Numerical Analysis, **17**, no. 2, 238–246, doi: 10.1137/0717021.

Gao, H., X. Wu, and G. Liu, 2021, ChannelSeg3D: Channel simulation and deep learning for channel interpretation in 3D seismic images: Geophysics, **86**, no. 4, IM73–IM83, doi: 10.1190/geo2020-0572.1.

Gao, K., 2024, Iterative multitask learning and inference from seismic images: Geophysical Journal International, **236**, no. 1, 565–592, doi: 10.1093/gji/ggad424.

Gao, K., and T. Chen, 2025, LATTE: open-source, high-performance traveltime computation, tomography and source location in acoustic and elastic media: Geophysical Journal International, **241**, no. 2, 1275–1326, doi: 10.1093/gji/ggaf079.

Gao, K., L. Huang, and Y. Zheng, 2022a, Fault detection on seismic structural images using a nested residual U-Net: IEEE Transactions on Geoscience and Remote Sensing, **60**, 1–15, doi: 10.1109/tgrs.2021.3073840.

Gao, K., L. Huang, Y. Zheng, R. Lin, H. Hu, and T. Cladohous, 2022b, Automatic fault detection on seismic images using a multiscale attention convolutional neural network: Geophysics, **87**, no. 1, N13–N29, doi: 10.1190/geo2020-0945.1.

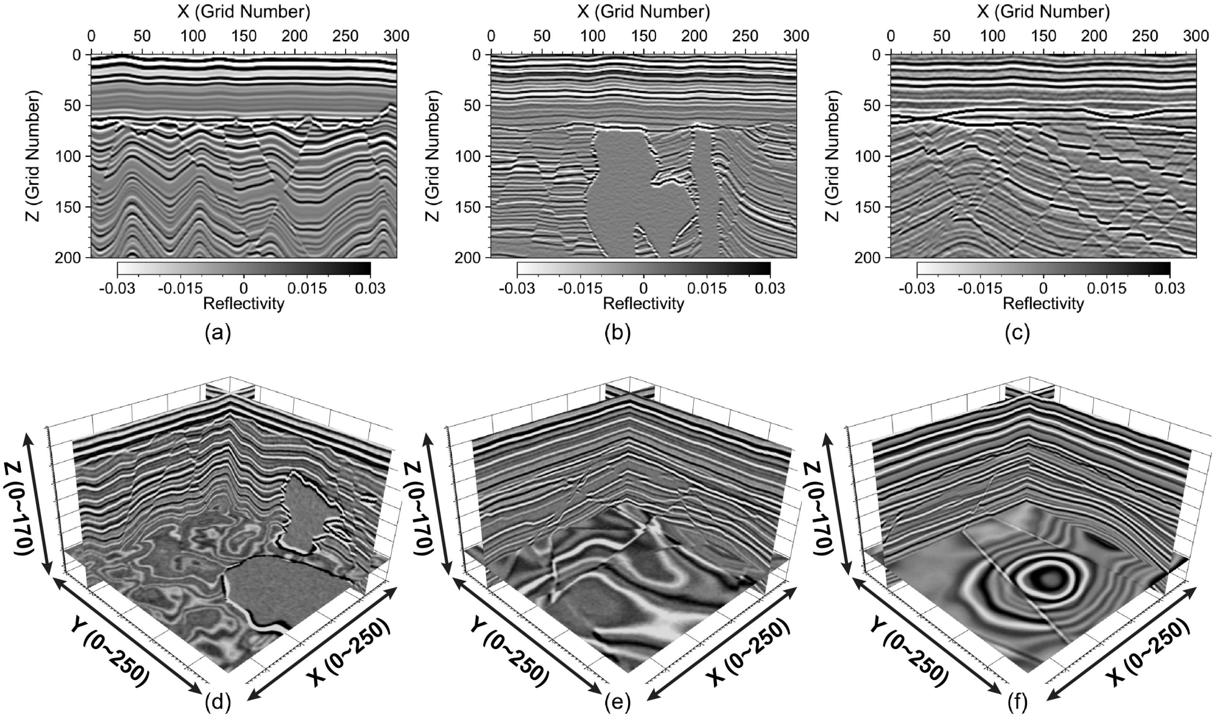

Figure 26: Examples of random geological models generated by RGM: (a-c) 2D and (d-f) 3D seismic images corresponding to the velocity models in Figure 24.

Gardner, G. H. F., L. W. Gardner, and A. R. Gregory, 1974, Formation velocity and density – the diagnostic basics for stratigraphic traps: Geophysics, **39**, no. 6, 770–780, doi: `10.1190/1.1440465`.

Geng, Z., X. Wu, Y. Shi, and S. Fomel, 2020, Deep learning for relative geologic time and seismic horizons: Geophysics, **85**, no. 4, WA87–WA100, doi: `10.1190/geo2019-0252.1`.

Georgsen, F., P. Røe, A. R. Syversveen, and O. Lia, 2012, Fault displacement modelling using 3D vector fields: Computational Geosciences, **16**, no. 2, 247–259, doi: `10.1007/s10596-011-9257-z`.

Grasemann, B., S. Martel, and C. Passchier, 2005, Reverse and normal drag along a fault: Journal of Structural Geology, **27**, no. 6, 999–1010, doi: `10.1016/j.jsg.2005.04.006`.

Guo, J., L. Xu, J. Ding, B. He, S. Dai, and F. Liu, 2021, A deep supervised edge optimization algorithm for salt body segmentation: IEEE Geoscience and Remote Sensing Letters, **18**, no. 10, 1746–1750, doi: `10.1109/LGRS.2020.3007258`.

Hudec, M. R., and M. P. Jackson, 2007, Terra infirma: Understanding salt tectonics: Earth-Science Reviews, **82**, no. 1, 1–28, doi: `10.1016/j.earscirev.2007.01.001`.

Laurent, G., G. Caumon, A. Bouziat, and M. Jessell, 2013, A parametric method to model 3D displacements around faults with volumetric vector fields: Tectonophysics, **590**, 83–93, doi: `10.1016/j.tecto.2013.01.015`.

Li, S., N. Liu, F. Li, J. Gao, and J. Ding, 2022, Automatic fault delineation in 3-D seismic images with deep learning: Data augmentation or ensemble learning?: IEEE Transactions on Geoscience and Remote Sensing, **60**, 1–14, doi: `10.1109/TGRS.2022.3150353`.

Lin, L., C. Li, H. Wei, Z. Zhong, X. Wang, Q. Li, and A. Gorman, 2025, An improved parametric 3D geologic modeling framework for seismic structure identification using deep learning in complex geologic settings: Geophysics, **90**, no. 3, IM81–IM102, doi: `10.1190/geo2024-0532.1`.

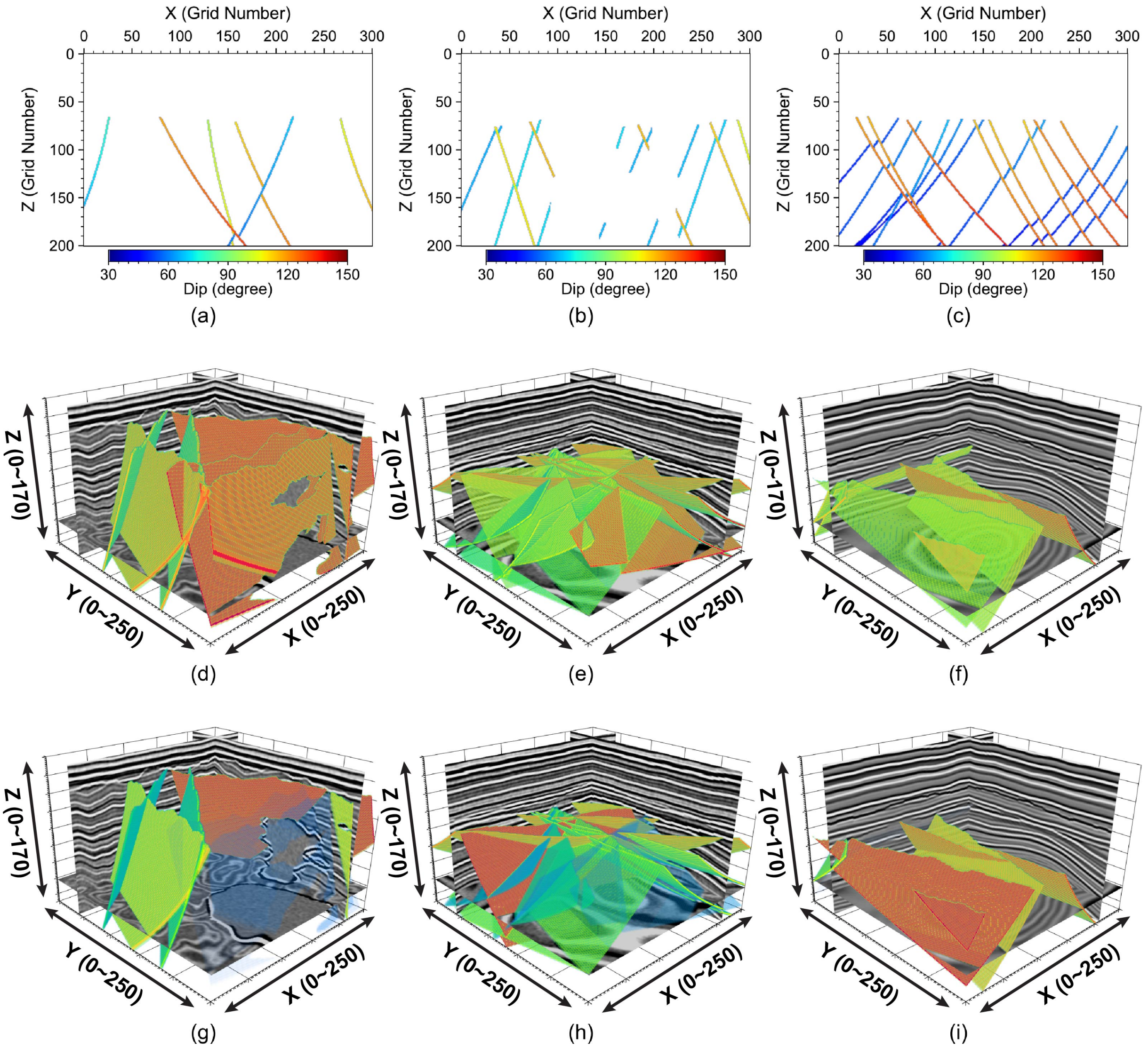

Figure 27: Examples of random geological models generated by RGM: (a-c) fault dip attribute in 2D models, (d-f) fault dip attribute in 3D models, and (g-i) fault strike attribute in 3D models corresponding to the velocity models in Figure 24.

Lin, L., Z. Zhong, C. Li, A. Gorman, H. Wei, Y. Kuang, S. Wen, Z. Cai, and F. Hao, 2024, Machine learning for subsurface geological feature identification from seismic data: Methods, datasets, challenges, and opportunities: Earth-Science Reviews, **257**, 104887, doi: `10.1016/j.earscirev.2024.104887`.

Perlin, K., 1985, An image synthesizer: Proceedings of the 12th Annual Conference on Computer Graphics and Interactive Techniques (SIGGRAPH ’85), 287–296, doi: `10.1145/325334.325247`.

Pham, N., S. Fomel, and D. Dunlap, 2019, Automatic channel detection using deep learning: Interpretation, **7**, no. 3, SE43–SE50, doi: `10.1190/INT-2018-0202.1`.

Shafiq, M. A., H. Di, and G. AlRegib, 2018, A novel approach for automated detection of listric faults within migrated seismic volumes: Journal of Applied Geophysics, **155**, 94–101, doi: `10.1016/j.jappgeo.2018.05.013`.

Tschannen, V., M. Delescluse, N. Ettrich, and J. Keuper, 2020, Extracting horizon surfaces from 3D seismic data using deep learning: Geophysics, **85**, no. 3, N17–N26, doi: `10.1190/geo2019-0569.1`.

Wang, S., Z. Cai, X. Si, and Y. Cui, 2023, A three-dimensional geological structure modeling framework and its application in machine learning: Mathematical Geosciences, **55**, no. 2, 163–200, doi: `10.1007/s11004-022-10027-9`.

Wang, S., X. Si, Z. Cai, L. Sun, W. Wang, and Z. Jiang, 2024, Fast global self-attention for seismic image fault identification: IEEE Transactions on Geoscience and Remote Sensing, **62**, 1–11, doi: `10.1109/TGRS.2024.3436066`.

Wu, Q., and H. Xu, 2003, An approach to computer modeling and visualization of geological faults in 3D: Computers & Geosciences, **29**, no. 4, 503–509, doi: `10.1016/S0098-3004(03)00018-9`.

Wu, W., Y. Yang, B. Wu, D. Ma, Z. Tang, and X. Yin, 2023, MTL-FaultNet: Seismic data reconstruction assisted multitask deep learning 3-D fault interpretation: IEEE Transactions on Geoscience and Remote Sensing, **61**, 1–15, doi: `10.1109/TGRS.2023.3299378`.

Wu, X., Z. Geng, Y. Shi, N. Pham, S. Fomel, and G. Caumon, 2020, Building realistic structure models to train convolutional neural networks for seismic structural interpretation: Geophysics, **85**, no. 4, WA27–WA39, doi: `10.1190/geo2019-0375.1`.

Wu, X., L. Liang, Y. Shi, and S. Fomel, 2019a, FaultSeg3D: Using synthetic data sets to train an end-to-end convolutional neural network for 3D seismic fault segmentation: Geophysics, **84**, no. 3, IM35–IM45, doi: `10.1190/geo2018-0646.1`.

Wu, X., L. Liang, Y. Shi, Z. Geng, and S. Fomel, 2019b, Multitask learning for local seismic image processing: fault detection, structure-oriented smoothing with edge-preserving, and seismic normal estimation by using a single convolutional neural network: Geophysical Journal International, **219**, no. 3, 2097–2109, doi: `10.1093/gji/ggz418`.

———, 2019c, Multitask learning for local seismic image processing: fault detection, structure-oriented smoothing with edge-preserving, and seismic normal estimation by using a single convolutional neural network: Geophysical Journal International, **219**, no. 3, 2097–2109, doi: `10.1093/gji/ggz418`.

Wu, X., Y. Shi, S. Fomel, L. Liang, Q. Zhang, and A. Z. Yusifov, 2019d, FaultNet3D: Predicting fault probabilities, strikes, and dips with a single convolutional neural network: IEEE Transactions on Geoscience and Remote Sensing, **57**, no. 11, 9138–9155, doi: `10.1109/tgrs.2019.2925003`.

Zhang, H., P. Zhu, Z. Liao, and Z. Li, 2022, SaltISCG: Interactive salt segmentation method based on CNN and graph cut: IEEE Transactions on Geoscience and Remote Sensing, **60**, 1–14, doi: `10.1109/TGRS.2022.3172997`.

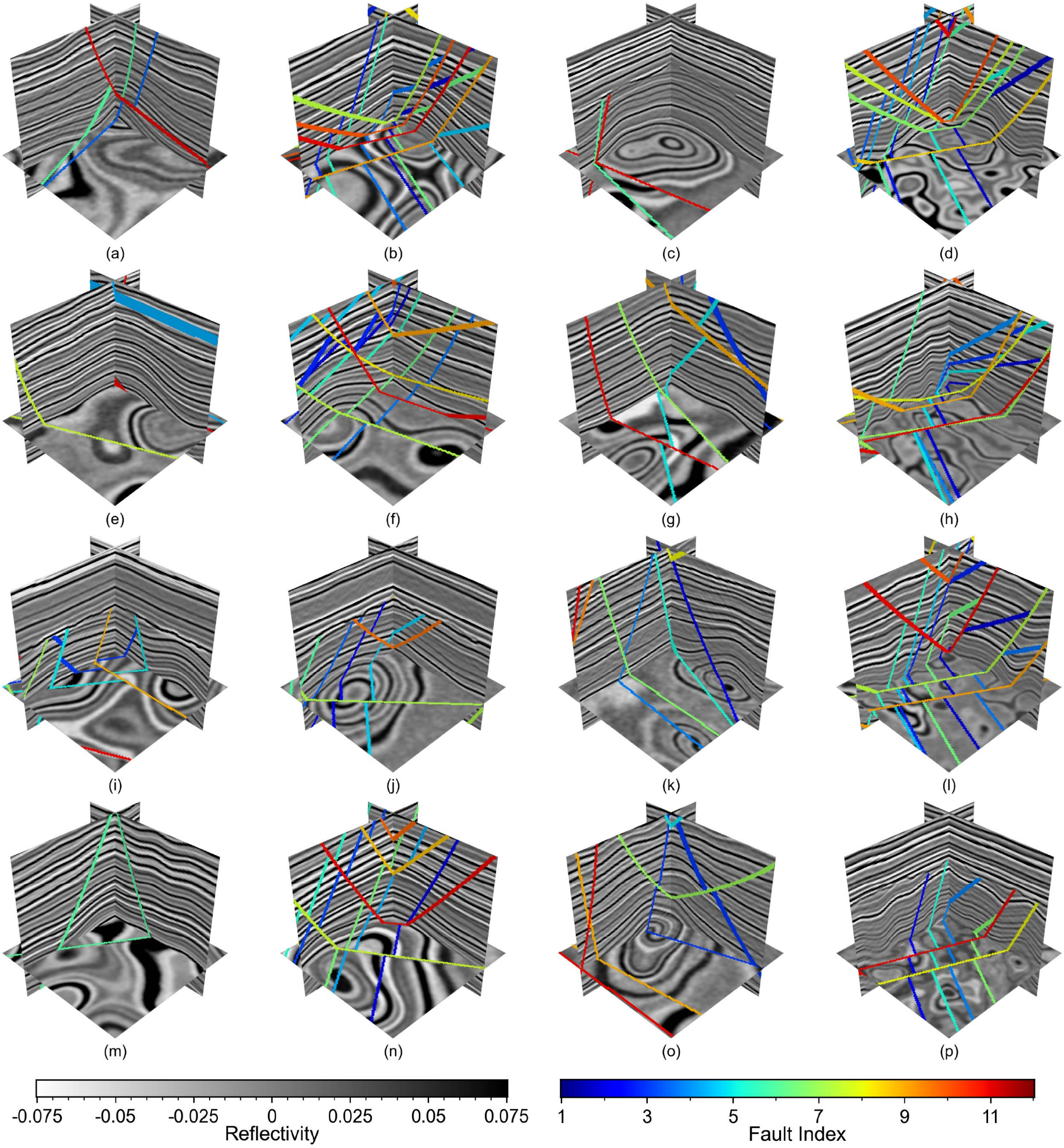

Figure 28: A total of 16 3D random geological models (images and fault index attribute) generated by RGM. Colors in these plots represent different faults (fault indices). For visual clarity, we plot the image slices without axes. All the images have a size of $128 \times 128 \times 128$ grid points.

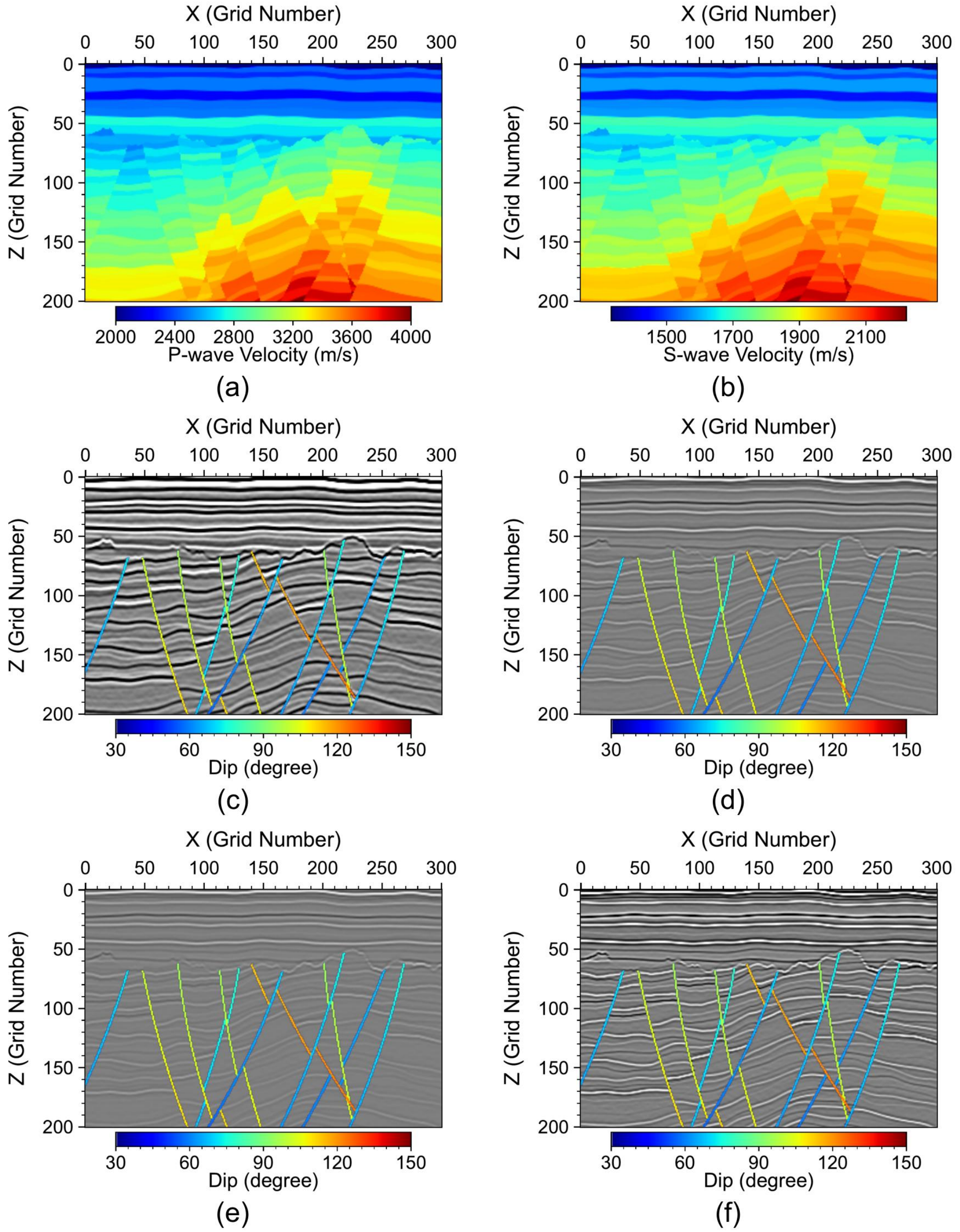

Figure 29: Examples of random geological models generated by RGM: (a-b) Random V_p and V_s models. (c-f) PP, PS, SP, and SS images corresponding to the velocity models in panels (a-b).